To the Graduate Council:

I am submitting herewith a thesis written by Matthew D. Parrish entitled "The Creation of Micropatterns through the Femtosecond Laser Ablation of Diamond Materials." I have examined the final electronic copy of this thesis for form and content and recommend that it be accepted in partial fulfillment of the requirements for the degree of Master of Science, with a major in Material Science and Engineering.

William H. Hofmeister, Major Professor

We have read this thesis
and recommend its acceptance:

Lloyd M. Davis

George M. Murray

Accepted for the Council:

Carolyn R. Hodges

Vice Provost and Dean of the Graduate School

(Original signatures are on file with official student records.)

The Creation of Micropatterns through the Femtosecond Laser Ablation of Diamond Materials

A Thesis Presented for

the Master of Science Degree

The University of Tennessee, Knoxville

Matthew D. Parrish

August 2009

Abstract

Laser systems that create nanometer and micrometer scale features on the surface of materials are important tools used by the scientific and industrial communities to develop novel applications and technology. The goal of the research presented in this thesis is to investigate the characteristics of a custom femtosecond micro and nano machining station that uses laser ablation to create features and to advance system capabilities. The improvements include programs that allow for a greater variety and complexity of features and patterns that are easily customized to specification. In this work, a titanium doped sapphire (Ti:S) laser oscillator and amplifier system operating at 800 nm and producing 200 fs pulses uses new designs to create features on the surface of two types of synthetic diamond samples: plasma enhanced chemical vapor deposited (PE-CVD) polycrystalline diamond and single crystal diamond grown by a high pressure, high temperature (HPHT) process. Several examples of new designs created by rotating and superimposing simple geometric shapes are presented as images acquired by a Scanning Electron Microscope (SEM). Included design improvements suggest that patterns with higher resolutions will experience a smoothing effect along jagged edges. The presented analysis of feature variation with power show that features created on single crystal diamond tend to be larger and deeper than those created on polycrystalline diamond at similar conditions. Overall, the measurements presented for both materials increase linearly with increasing power. Also, the designs are best emulated by features ablated at relatively low powers. Raman spectroscopy shows that neither the single crystal diamond nor the polycrystalline diamond undergoes graphitization due to either single pulse or high repetition rate femtosecond ablation processes.

Table of Contents

List of Figures

1. Introduction

Lasers have been used for academic and scientific research for almost fifty years. The development of a class of lasers producing extremely short pulses, called ultrafast lasers, has increased the laser's utility even further. The femtosecond laser is better for machining patterns than longer pulse lasers because most surface damage due to thermal effects is avoided. This is because the short femtosecond laser pulse transfers its energy to the material far faster than the energy can diffuse away and damage the lattice [1].

Laser ablation systems are also excellent alternatives to other competitive forms of micropatterning technology like traditional tool machining, chemical wet etching, focused ion beam etching, reactive ion etching, and plasma etching. Patterning by laser ablation avoids the tool wear experienced by traditional machining tools [2]. Laser ablation systems are economical and flexible and do not require photomasks, the handling of corrosive acids, or a cleanroom environment for operation. Furthermore, ion implantation and contamination due to processing are also avoided. Patterns can be created quickly and in two or three dimensions, unlike some of the other techniques mentioned [3, 4]. In some cases, laser machining can create complex structures and patterns that are just not possible with other techniques [5].

Femtosecond lasers with appropriate parameters can alter materials through a process called ablation to create features on the surface with dimensions on the micrometer scale. Many research groups have investigated the theory of ablation for specific materials and general material groups such as metals and dielectrics [6-9]. Femtosecond laser ablation is compatible with many materials [10-14]. Because diamond is a well known material with many desired electrical, chemical, and mechanical properties [15, 16], the processing of diamond could lead to many novel technologies [17].

The laser ablation community is investigating several materials, including diamond, for practical use in various fields of research. Among the most popular applications are passive microfluidic devices like channels, reservoirs, and through-holes in various materials [5, 18, 19], optoelectronic devices like waveguides in dielectric materials [20-22], electron emitting devices for high speed or high power electronics created from diamond or diamond-coated materials [23-25], diamond tools like industrial cutters and scalpels for surgery [26, 27], and biomedical and chemical applications involving small channels [3, 28]. Overall, there are many possible avenues of research to pursue. In each of these presented fields of research, the quality of feature design and material ablation is of extreme importance to the development of applications. Similar to how these applications require complex designs to become realized, our own feature creation system required expansion to advance our own scientific inquiries.

This work discusses the overall feature creation system and the improvements made to increase the variety and complexity of available designs for pattern and feature ablation. Chapter 2 discusses important aspects of ablation theory like mechanisms and relevant timescales. Chapter 3 presents details concerning the laser source that produces the material ablation, the control and design programs, and other experimental procedures. Chapter 4 exhibits the results of this research, including examples for different design types and materials, a few design improvements, a simple analysis of feature variation with increasing laser pulse energy, and the results of Raman spectroscopy performed on ablated and un-ablated regions.

2. General Ablation Theory

2.1. Ablation Mechanisms

Though dielectric materials do not normally conduct a current, they can be forced to conduct under the right conditions. This change in the material's properties and behavior is called a breakdown and can lead to material damage, a permanent change in material properties, or the removal of material. Lasers may utilize this material breakdown by targeting a sample with a laser's output of appropriate wavelength and temporal duration. When using lasers, the breakdown is due to the interaction of the material with the light radiation and is called optical breakdown.

High laser pulse intensities focused onto incredibly small areas can create the electric field strength required to cause ionization. When irradiating the sample material, the laser pulse transfers its energy to the electrons through a nonlinear photoionization method. As discussed by Schaeffer et al. [29] and shown in Figure 1, the free electrons are produced by one of the nonlinear photoionization methods of tunneling ionization, multi-photon ionization, or a combination of both of these. Any free electrons produced by tunneling escape with the aid of the laser radiation due to the resulting suppression of the electric field strength that binds the electrons to the valence band. Free electrons produced by multi-photon ionization simultaneously absorb energy from several separate photons to overcome the binding electric field strength. Regardless of the mechanism producing the free electrons, these electrons gain kinetic energy within the laser's electric field and can collide with bound electrons. If enough energy is transferred during the collision, the bound electrons will be freed. This process is called impact ionization and will continue to exponentially create more free electrons through multiple iterations in a process called avalanche ionization. Figure 2 exhibits the absorption of

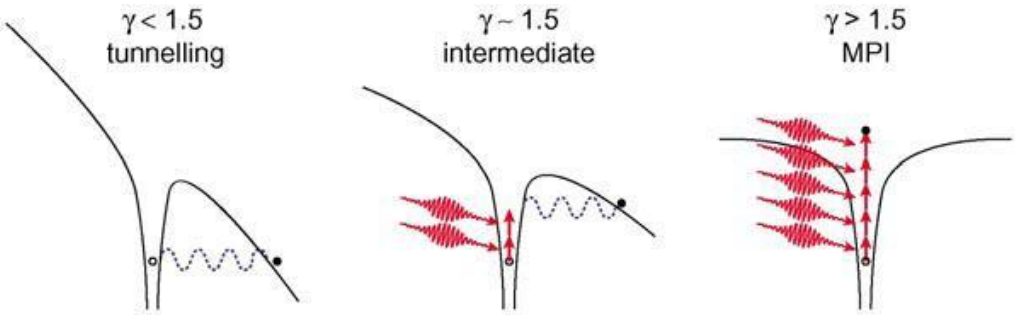

Figure 1. Nonlinear photoionization mechanisms. Illustration of three divisions of nonlinear photoionization modes as described by calculations of the Keldysh parameter γ . Values shown correlate to Shaeffer's expression of the Keldysh parameter. The red line represents photon absorption while the black dotted line represents a tunneling electron. The solid black lines represents the strength of the electric field containing the bound electrons [29].

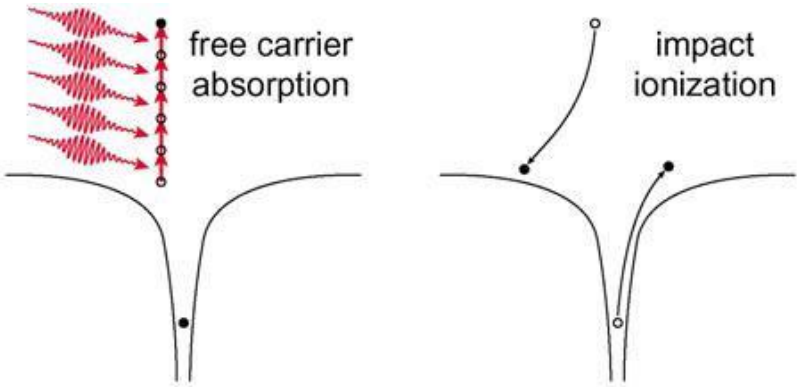

Figure 2. Avalanche ionization. This illustration shows a free electron absorbing energy from a photon. The energetic free electron collides with a bound electron to result in two free electrons with low energy. The process repeats to cause avalanche ionization over many iterations [29].

photon energy by a freed electron and the resulting collision between a free and bound electron [30].

Once enough free electrons are produced, the section of the material targeted by the laser behaves like a plasma; it responds to electric fields and has a very high electrical conductivity. Once the free electron density reaches the critical value of 10^{22} cm^{-3} to 10^{23} cm^{-3}, the electrons behave as a plasma that has a natural frequency of oscillation that resonates with the laser and efficiently absorbs and reflects the laser pulse energy. Coulomb repulsion between like charges causes a quick expansion of the local plasma in the form of a plume. This rapid expansion resembles an explosion and a shock wave is created within nanoseconds of irradiation. The plasma expansion may be visible as a spark and the shock wave may be audible. The final results of laser-induced optical breakdown may include permanent material damage, altered material properties such as the index of refraction, or even the removal of material known as ablation [30].

2.2. Timescales and Models

Femtosecond duration pulses are attainable due to the unique design of mode-locking ultrafast lasers. Lasers produce light that is not of a single frequency, but created from several frequencies within a range called a bandwidth. The range of frequencies that the laser may actually operate within, called the gain bandwidth, is due to the combination of the laser gain medium and the resonant optical cavity. The optical cavity allows the light to reflect continuously and constructive interference creates standing waves or longitudinal modes within the cavity. These modes are the only frequencies that can undergo oscillation in the resonant

cavity. The laser output spectrum constitutes only the longitudinal modes created by the resonant cavity which are also supported by the gain bandwidth of the selected gain medium. The energy-time description of the uncertainty principle says that a state that exists for only a short time will not have a definite energy. In other words, extremely short pulses must contain an output spectrum containing a wide range of wavelengths. Therefore, a femtosecond laser will require the selection of a gain medium that has a large gain bandwidth. The solid-state titanium-doped sapphire crystal is a widely used gain medium for ultrafast lasers and has a bandwidth of 128 THz or 300 nm centered around 800 nm. The constructive interference of the modes supported by the gain medium and the optical cavity produces a femtosecond pulse with each oscillation of the laser light. Also, the energy of the pulse has an increased chance to be absorbed by target materials because each pulse is a combination of many frequencies of light.

As shown in Figure 3, there are several timescales of interest when a material is ablated by a femtosecond laser pulse. Energy is transferred to the electrons at the beginning of the pulse by nonlinear photoionization mechanisms within 10-100 fs. Later in the femtosecond pulse, impact and avalanche mechanisms increase the free electron density to the critical value discussed above on the timescale of 10 fs to 10 ps. Throughout the femtosecond pulse, some of the energy absorbed by the electrons is transferred to the lattice by carrier-phonon scattering on the timescale of 100 fs to 10 ps. The shockwave created along with the plasma expansion propagates from approximately 50 ps to a few ns. Thermal diffusion occurs around the picosecond timescale and solidification of molten areas can occur from nanoseconds to microseconds after irradiation [30].

Models have been developed to describe various aspects of the ablation process. One useful relationship describes which type of nonlinear photoionization is responsible for the

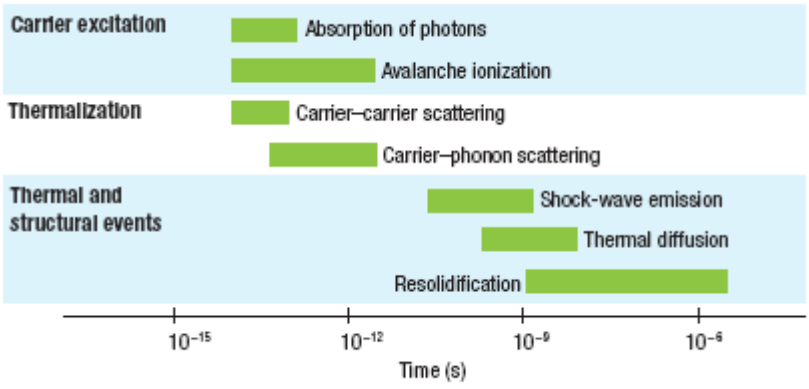

Figure 3. Timescale of femtosecond ablation. This chart shows the various timescales involved when ablating a material with a femtosecond laser pulse. The absorption of energy absorption occurs much faster than the occurrence of thermal effects [30].

creation of the initial free electrons during ablation. Whether multi-photon absorption or tunneling ionization predominates is described by the Keldysh parameter, γ, in the following expression: $\gamma = \sqrt{IP/(2*UP)}$. In this equation, IP is the ionization potential and represents the amount of energy required to ionize the targeted material. Because the laser field is inhomogeneous, each oscillation causes an electron's final position to be slightly different from its initial position. A net force is created and the electron experiences a gain in energy called the ponderomotive energy, or UP. For this expression, multiphoton ionization dominates the creation of the free electrons when the Keldysh parameter is greater than 1. If the Keldysh parameter is less than 0.5, then tunneling dominates. However, if the value is between 0.5 and 1, then both mechanisms attribute to the density of free carriers. Models like Perelomov-Popov-Terent'ev (PPT) [31] can successfully describe situations involving a single electron. Higher-order ionization processes can be described by models once the dynamics of ionized electrons

are considered within each cycle of oscillation. One such model, the re-collision model, suggests that collisions can cause an ionized electron to recombine with its parent ion or scatter off the parent ion to produce more free electrons. According to the model, if collisions between electrons and local atoms are prevalent, then collision-assisted multiphoton ionization (CAMPI) [32] will be significant in the ionization process. It was observed that the Keldysh photoionization rates necessary for damaging the material accurately correlate with the measured damage threshold when ablating within the material bulk. However, on the material surface, the photoionization rates are significantly less than those described by the Keldysh photoionization rates. It is during the irradiation of the material's surface that the unrestricted plasma expansion is the cause of material ablation and the machining of micropatterns [33].

The temporal duration of the laser pulse is an important parameter in material ablation. At durations around 200 fs, impact ionization and nonlinear photoionization have a comparable contribution to the density of free electrons. As the pulse duration increases, impact and avalanche ionization create more of the free electron population than nonlinear photoionization by using free electrons already available within the material. Because the mechanism depends on the original, random amount of electrons, the threshold of optical breakdown is less deterministic when compared to the threshold of the femtosecond pulse regime. At temporal durations of 50 fs, impact and avalanche ionization do not supply a noticeable amount of free carriers due to the electrons' inability to absorb the laser energy quickly enough. Instead, another mechanism similar to CAMPI called collision-assisted multiphoton avalanche is important in generating the electrons at this pulse duration. In order to release bound valence electrons, this mechanism requires the absorption of energy from photons and colliding

conduction band electrons with low energies. Similar to normal avalanche ionization, this process increases in probability as the free electron density increases [33].

2.3. Comparison of Femtosecond and Nanosecond Pulses

The timescales of interaction given earlier are for a femtosecond laser pulse. In general, nanosecond, picosecond, and femtosecond laser ablation are similar but with a few important differences. Nanosecond and longer pulses create several types of thermal damage such as spatter, recast layers, heat affected zones, and microcracks. When compared with nanosecond pulses, ultrafast laser pulses mostly or completely eliminate material damage by these thermal processes [3, 34]. Another difference between the ns and fs regimes involves the ablation of different types of materials. For nanosecond pulses, the ablation of metals occurs at a much lower intensity than the ablation of dielectrics, which have low absorption. Femtosecond ablation, however, occurs consistently regardless of material type. The elimination of thermal damage and the consistency of ablation for different materials are both due to the interaction timescales involved between the electrons and the ions of the material's lattice. Since the carrier-phonon scattering timescale is of picoseconds, the electrons have plenty of time to receive energy from a ns laser pulse and transfer it to the lattice ions, causing a near equilibrium condition [30]. The final results of ns ablation are thermal diffusion, expansion, and material damage. Femtosecond laser pulses, however, span a tiny fraction of time when compared with the carrier-phonon scattering timescale. The laser pulse transfers energy to the electrons much faster than the electrons can convey the energy to the surrounding lattice atoms [33]. The result of fs ablation is a material without the characteristic nanosecond thermal damages. This is why ultrafast ablation is preferred in the development of many novel applications [8, 35].

2.4. Ablation Dependence on Physical Parameters

It is understood that nonlinear photoionization and avalanche ionization are the processes by which lasers transfer energy to a material. If the bandgap of the material requires an electron to absorb N number of photons to escape the conduction band, then the probability of absorbing the necessary energy through only nonlinear processes depends on the electric-field intensity of the laser, I, as I^N. If nonlinear ionization was solely responsible for the transfer of energy, then the intensity required for material alteration would depend on the material's bandgap and vary greatly between different materials. Experiments show that the threshold of intensity for ablation, I_{TH}, is only mildly influenced by the material's bandgap energy. This is due to the linear dependence of avalanche ionization on the laser intensity and implies the importance of avalanche ionization in the ablation process. Femtosecond laser ablation can be used on a wide range of materials regardless of a large or small bandgap as a result of the involvement of avalanche ionization [30].

The threshold intensity of light required for the ablation of materials, I_{TH}, is determined by such experimental parameters as the laser pulse duration, τ, the laser pulse energy, E, and the numerical aperture of the objective, NA. The dependence of I_{TH} on the laser pulse duration has been investigated for pulses as short as tens of fs. Two different behaviors of the τ dependence are observed, neither of which comply with the inverse relationship expected. For pulse durations greater than 10 ps, the intensity dependence is $\tau^{1/2}$ and the material damage is a result of the Joule heating of electrons during the initial part of the pulse. For pulse durations shorter than 10 ps, the value of I_{TH} cubes with every order of magnitude increase of τ. Overall, the weak dependence of I_{TH} on τ is due to the linear dependence of avalanche

ionization on the electric-field intensity. Though nonlinear photoionization initially creates some free electrons, avalanche ionization is responsible for using these seed electrons to create the necessary electron density for ablation [30].

The pulse energy, E, required by nonlinear photoionization processes to create seed electrons is called the threshold energy. If a E near the threshold energy is used, then the absorption of radiation may result in a change in the material's index of refraction within the irradiated area. The resulting changes in refractive index are of the same order of magnitude as used in standard optical fibers but are not spatially uniform. By increasing the pulse energy above the threshold energy value, the size of the affected area and the average energy of the plasma will both increase. Higher plasma energy will cause greater Coulomb repulsion, eventually with enough energy to create the formation of voids and leave behind micromachined features [30].

Laser ablation systems typically use an objective lens to focus the laser energy onto a small area of the sample. The numerical aperture of the objective lens, NA, determines the width of the focal volume for laser irradiation. A minimum NA of 0.002 is required to achieve the threshold intensity using millijoule pulse energies. However, the minimum NA is practically 0.1 because the transfer of energy to the material below this value is disrupted by the nonlinear optical effects of self-focusing and white light generation. Below a NA of 0.1, the threshold for these nonlinear processes is below I_{TH}, and machined features are more difficult to accurately reproduce. For a NA around 1 and greater, the micromachining of glass is possible by using nano pulses. Due to the focusing objective, the energy delivered by many laser pulses collects in a small area faster than it can diffuse throughout the lattice. Once the diffusion of this energy begins, it behaves as a source of heat and creates features on the micro and nano scales that are

significantly larger than the original focal volumes designated by the objective's numerical aperture. A high *NA* will set the threshold energy and the size of the resulting feature will depend on the number of pulses. For single shot laser pulses, a *NA* of 0.6 and higher creates nearly spherically symmetric features. Below a *NA* of 0.6, the features are larger and form asymmetrically [30].

2.5. Incubation Effect and Models

An experimental observation known as the incubation effect is of importance to laser ablation with multiple laser pulses. As shown in Figure 4, the incubation effect is a trend for the threshold fluence required to damage a material to decrease with an increase in the number of pulses. In one experiment, the threshold fluence for a material irradiated by 1 laser pulse is 1.5 J cm^{-2} while the threshold fluence for 2000 laser pulses is significantly less at 0.5 J cm^{-2}. By increasing the number of pulses, the surface is altered slightly by each pulse and the absorption of the laser energy increases as a result. With a large increase in the number of pulses, such as the example above, the difference in the threshold fluence is noticeable. The incubation effect has been observed for several types of materials in experiments with laser pulse durations ranging from femtoseconds to nanoseconds [34].

There are two models which describe the incubation effect and its interaction with materials. One model proposed by Jee et al. [36] suggests that some of the energy deposited by the laser pulses causes plastic strain within the material through thermal effects. Though the model originally explained the irradiation of copper with nanosecond pulses, it can also be applied to the ablation of metals, ceramics, and polymers by femtosecond pulses. Many thermal

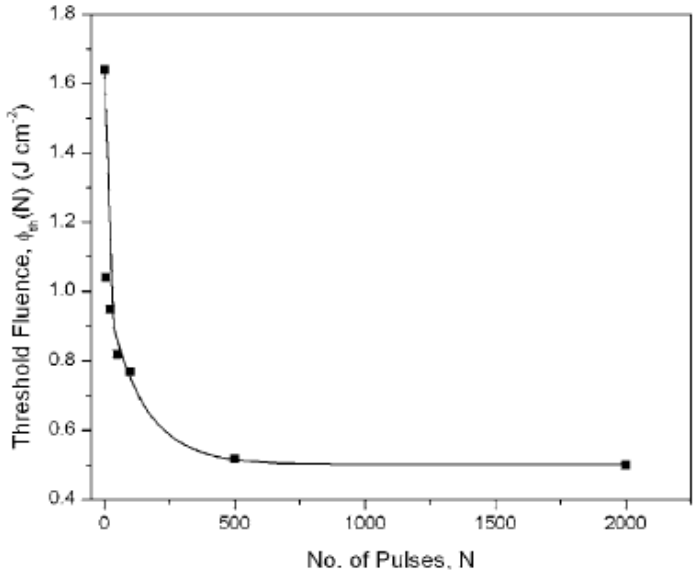

Figure 4. Incubation effect. The incubation effect is when the threshold fluence required to damage the material decreases as the number of incoming pulses increases [34].

effects have been suggested to be the operating incubation mechanism for metals and ceramics, including induced plastic strain, recrystallization, amorphization, oxidation, and increased surface roughness. Of these effects, the increased absorption of energy is thought to be due to the alteration of the surface roughness by irradiation because it is the only mechanism that applies to both ceramics and materials. A single mechanism for the increased absorption of laser energy is consistent with experiments because evaluated metals and ceramics behave similarly within the model [34].

A different model proposed by Ashkenasi et al. [37] was developed through studying the femtosecond ablation of dielectric materials. It assumes that the decrease in threshold intensity with an increasing number of pulses is due to the creation and accumulation of defects within the ablated material area. The defects are generated by the laser and include self-trapped excitons, Frenkel electron-hole pairs, and color centers. The threshold intensity undergoes a drastic decrease with an increase to a few pulses but then stabilizes over a large number of pulses [34].

Though both models describe the rapid decay of the intensity threshold with an increasing number of pulses, there is a preference for which model should be adopted. The first model, proposed by Jee et al., is preferred when a range of several hundred pulses are involved or when high fluences are considered. The second model, proposed by Ashkenasi et al., should be used when dielectrics are irradiated near the single-pulse threshold fluence. Choosing the correct model ensures that the true causes of the incubation effect correlate to the current experimental material type and fluence level [34].

3. Experimental Setup

3.1. Laser System

In this work, laser pulses of femtosecond duration are created by a system consisting of three solid-state laser modules: an energy pump, a laser oscillator, and a laser amplifier. The system was purchased and assembled by the Center for Laser Applications at UTSI. Postdoctoral fellow Yelena White was responsible for implementation with the assistance of Alexander Terekhov. Diagrams of this system are presented in Figures 5 and 6. The energy pump, Verdi V18 from Coherent, Inc., is a diode-pumped frequency doubled Neodymium-doped Yttrium Orthovanadate (Nd:YVO_4) solid-state laser. This laser provides continuous output of laser energy to the oscillator and amplifier at 532 nm. The laser oscillator, Tsunami from Spectra-Physics, Inc., is a regeneratively mode-locked laser using a sapphire crystal (Al_2O_3) doped with titanium (Ti:S or Ti:Saph). This module absorbs the energy pumped from the Verdi module and creates a mode-locked steady-state to emit ultrafast laser pulses on the femtosecond time scale. The third module, RegA 9000 from Coherent, Inc., is a Ti:S regenerative amplifier. RegA takes the output pulses from the Tsunami oscillator and amplifies them over a thousand times with the aid of the Verdi pump laser to produce the final output of the system. The resulting pulses have energy around 4 μJ, a wavelength around 800 nm, and temporal widths of 200 fs. This system has as average output of 1 W and can be programmed to produce either single pulses or pulse repetition rates as high as 250 kHz.

Optical equipment, a focal objective, and the use of mobile stages relay the laser output for material ablation to the target sample located in the delivery system. The delivery system was designed and assembled by Dr. Othman Zalloum and Alexander Terekhov. Zalloum aligned and maintained the Raman beam path while Terekhov did likewise for the ablation beam path.

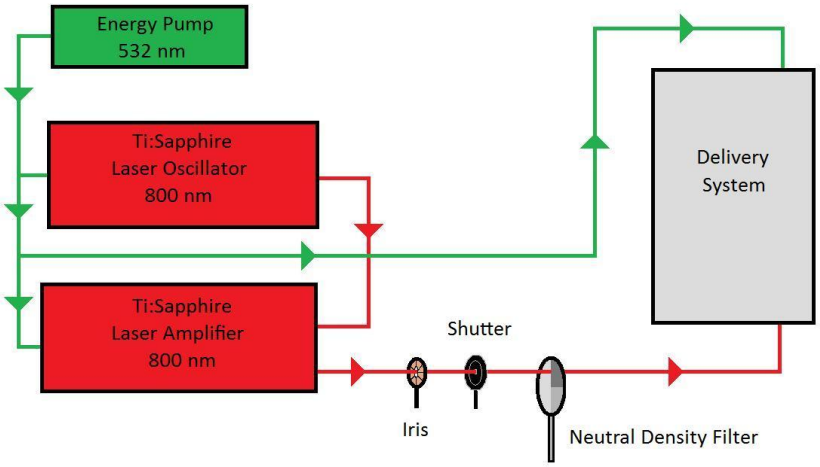

Figure 5. Diagram of laboratory setup. The laser modules are represented by the green and red blocks. The beam paths for ablation and Raman are represented by red and green lines and the flow is indicated by the direction of the triangles. Both paths are directed to the beam delivery system.

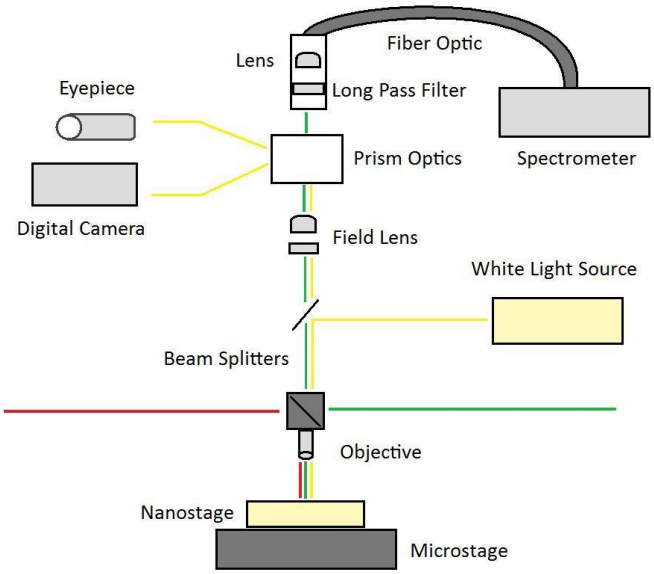

Figure 6. Diagram of the delivery system. The laser system's output is directed towards the target material placed on the nanostage surface. The ablation and Raman beam paths are represented by red and green lines. A white light source is represented by the yellow beam path.

An externally triggered shutter directs the ablation time for experiments involving high repetition rates. A neutral density filter placed within the beam path is used to adjust the beam's power. A 100 X microscope objective, MPlan DIC Dry 210/0 from Nikon, focuses the laser energy onto the material surface to create the necessary fluence for ablation. This objective has a numerical aperture of 0.90 and a spot size radius of approximately 0.55 microns. The objective has a working distance that is less than 1 mm and is mounted on a stage where the user adjusts the Z direction to find the correct focus for ablation. The delivery system allows for direct viewing during material ablation through a 10 X eyepiece or a high resolution digital camera, C8484-05 from Hamamatsu, relaying images to a computer monitor. In the past, two other objectives were used in the ablation process. The two old objectives, NPL 100 X 0.90 ∞/0 from Leitz Wetzlar and U M Plan FL 100 X 0.90 BD ∞/0 from Olympus, had similar properties to the current objective selected.

The spot size correlating to the ablation objective was estimated by a procedure involving a standard microscope objective calibration target, OB-MM from Olympus. The target has a total length of 1 mm and is equally divided into one hundred divisions of 10 μm per division. While blocking the laser, we used the digital camera to capture an image focused on the surface of the calibration scale illuminated by the lamp. An additional image was taken of the illuminated surface of a sample material while the laser ablates at a very low irradiance. This image is actually a measure of the irradiance versus X-Y location within the plane of the spot. This data is graphed and the spot size is calculated as the radius of the beam at the level of $1/e^2$ multiplied by the maximum irradiance. This spot size calculation is then compared with the image of the calibration scale to estimate the dimension of the spot size. For this measurement and ablation, the procedure of selecting the focus for ablation by setting the focus of the eyepiece

on the sample surface may not provide for the actual best focus. The actual spot size may be less than approximated by the above technique and the surface of a targeted sample may not precisely correlate with the center of the beam's depth of focus. However, the surface-focusing technique was consistently used in this research and resulted in the creation of the micropatterns presented in this work.

The sample is placed under the objective by the use of two stacked mobile stages. The sample is placed directly on the top stage, a piezoelectric stage from Mad City Labs, Inc., which has nanometer precision throughout a range of 200 microns horizontally in the X and Y directions and vertically in the Z direction. The bottom stage is from McBain, Inc. and uses Compumotor, Inc. stepper motors with National Instruments motor drivers. The McBain stage has a large range of motion across the X and Y directions and is used for the general positioning of the sample by moving both stages and the sample as one object. During ablation, the microstage is inactive and the nanostage scans at 11 μm/s to create the micropatterns. Typical ablation parameters include 3 ms of ablation duration per ablation site with three passes for designed features or a single pass for arrays of holes.

Raman spectroscopy is a powerful tool that can indicate if a diamond material has changed to graphite by comparing scans taken before and after the ablation process. For this integrated laser ablation/Raman spectroscopy setup, the 532 nm output of the Verdi V18 module is used as the Raman source. Raman spectroscopy is performed using a 60 X objective with a numerical aperture of 0.85 and a working distance less than 1 mm. The Raman signal scattered by the surface is collected by the Raman objective, focused into a multimode fiber optic, and carried by the fiber to a spectrometer, QE65000 from Ocean Optics, Inc.. The spectrometer is equipped with a two-dimensional charge coupled device (CCD) detector which has 1044 x 64

total pixels and a high signal-to-noise ratio. The dynamic range of the spectrometer can be increased by longer integration times and spectral averaging. The detector's valid range for Raman shift is between 200 and 2670 cm^{-1}. Some of the laboratory equipment used in this laser ablation/Raman spectroscopy system is displayed in Figures 7-9.

3.2. LabVIEW™ Programming

Two programs created by Dr. William Hofmeister with the LabVIEW™ software package control the movement of the two stages throughout the ablation process. The microstage program allows the user to direct the movement of the microstage in the X and Y directions at various velocities. It also displays the current lateral position of the microstage and allows for adjustments to the current focus position by controlling the motion of another stage along the Z direction.

The nanostage program is the second LabVIEW™ program and is responsible for designing and creating the micropatterns. Several tabs in this program correspond to the various types of micropatterns available. The array tab designs a grid of points where the intersections of the rows with the columns are designated ablation sites. The treepan tab allows circular patterns to be ablated with a specific number of points distributed along the circle's circumference. The Excel™ tab imports data from Excel™ files into LabVIEW™. Two columns in the file list the ablation site as coordinate positions and another column lists the intended duration for ablation. LabVIEW™ previews any currently designed pattern as a graph as it will appear on the sample. Examples of array, treepan, and Excel™ patterns created by the nanostage program are displayed in Figures 10-12. After initiation, the program moves the nanostage to create the designed pattern while the laser is ablating.

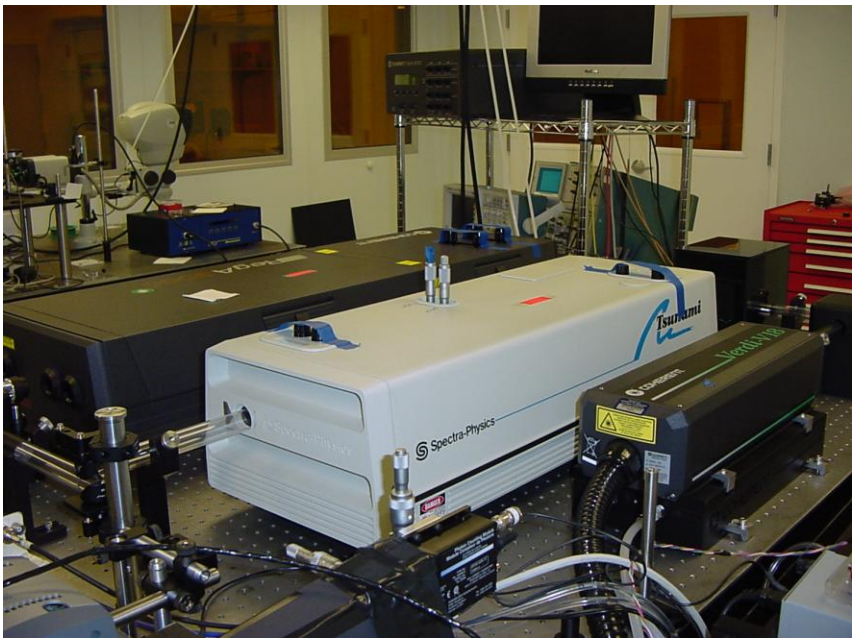

Figure 7. Laser modules. The Verdi V18 energy pump is on the right, the Tsunami laser oscillator is in the middle, and the RegA 9000 laser amplifier is on the left. These three modules comprise the laser system.

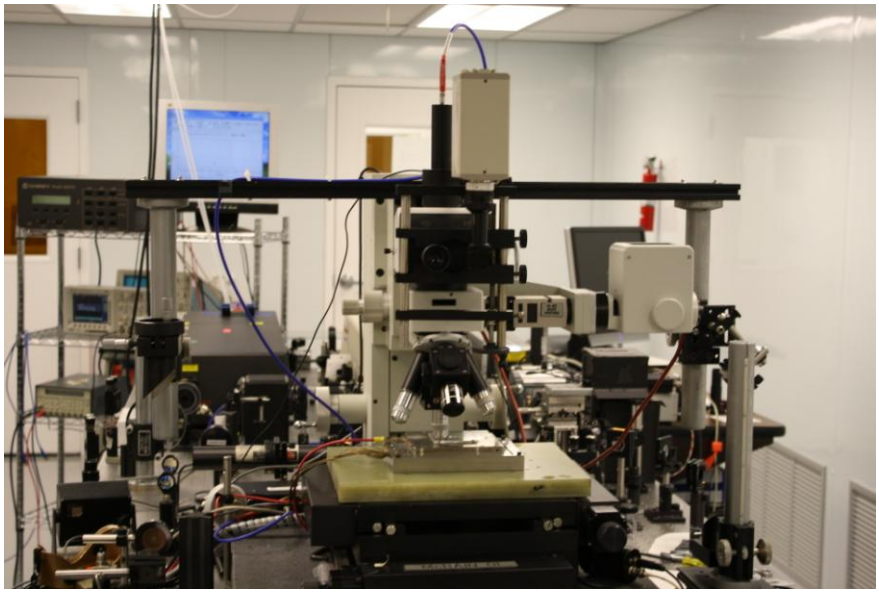

Figure 8. Delivery system. The delivery system is designed to relay the two beam paths through the objective attached to the central platform. The platform rotates to allow the use of the other objectives in the delivery system. The lamp, 10 X eyepiece, digital camera, CCD detector and both stages are displayed. The microstage is the black, lower stage and the nanostage is the metallic, upper stage.

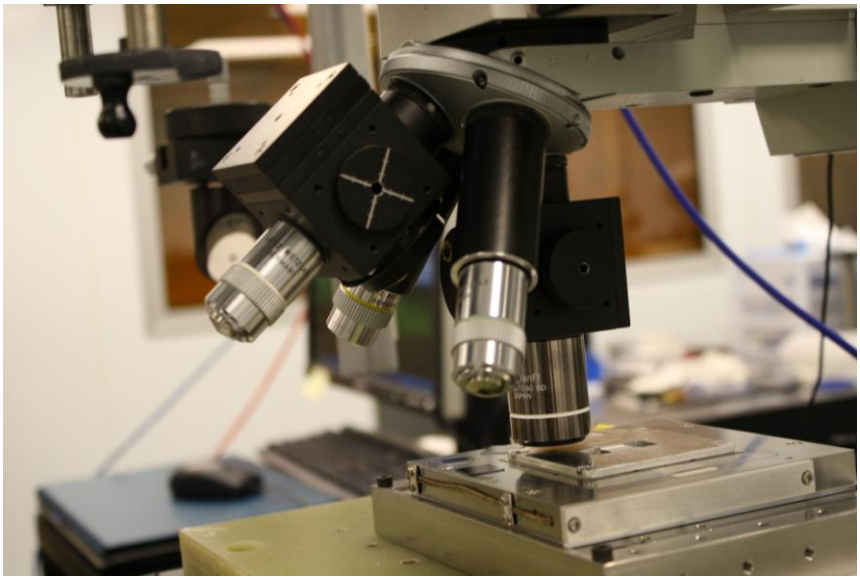

Figure 9. Objective platform. The objective platform and nanostage are visible. The setup delivers the laser output to the small hole located on the side of the black box housing the objective. The sample to be ablated is placed on the nanostage under the preferred objective.

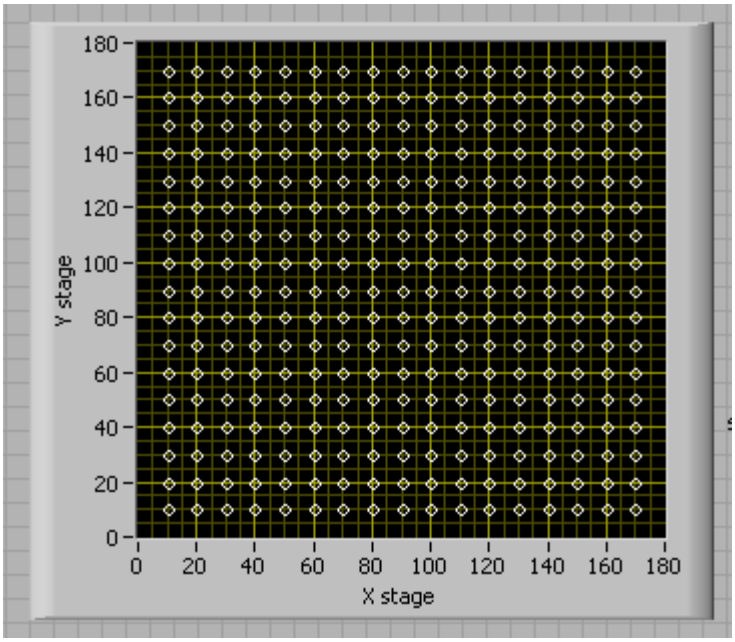

Figure 10. Array of holes design. This array design has 17 rows and 17 columns with a distance of 10 μm between any two of the 289 adjacent ablation sites.

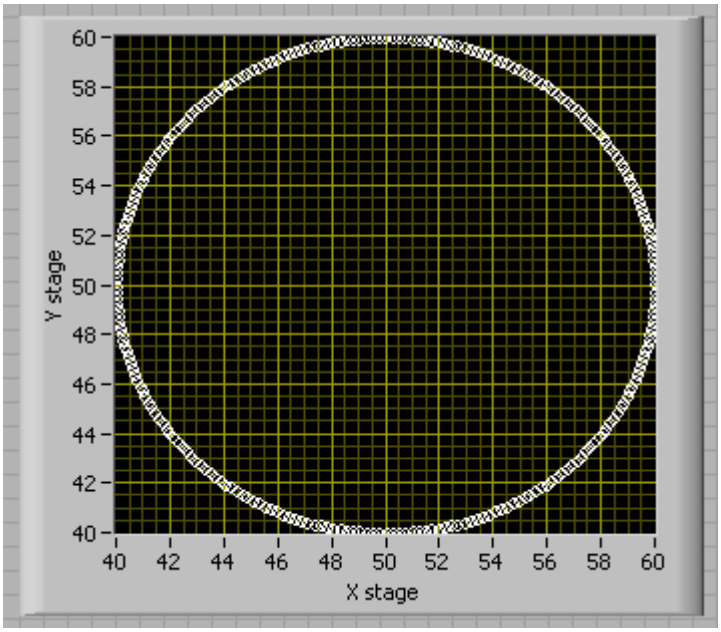

Figure 11. Treepan design. This treepan design has a radius of 10 μm and 256 ablation sites distributed along the circle's circumference with a distance of 245 nm between adjacent sites.

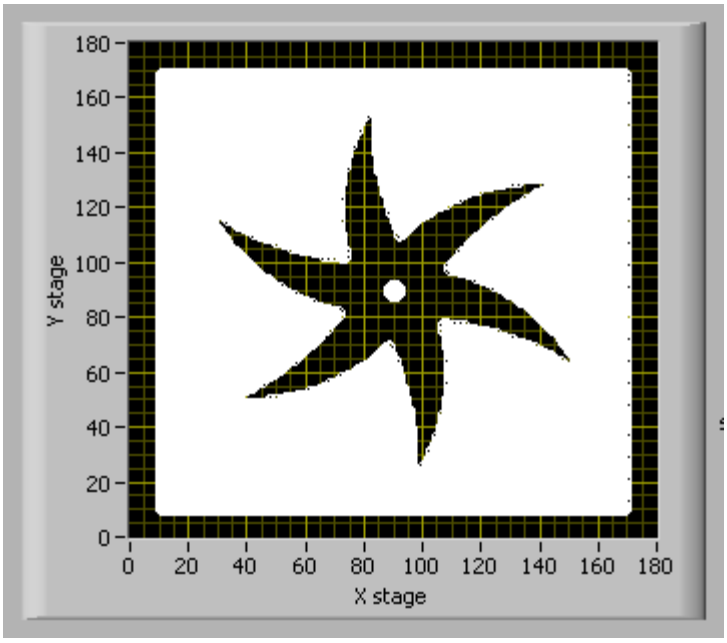

Figure 12. Micropattern design. Ablation of the white space in this image will create a star with six curved spikes and a small hole in the center. The spikes are separated by 60 degrees.

3.3. Design Programs and Algorithms

New programs were required to increase the limited number of patterns available for ablation. Richard Thompson created these new programs using Visual Basic™ from algorithms that the author developed on paper. Specifications for the shapes and patterns were designed and Thompson's program created the files that were imported into LabVIEW™ as an Excel™ file by the nanostage program. The programs create designs in two ways: either by creating solitary or superimposed combinations of simple shapes or by symmetrically rotating and overlaying a simple shape at multiple angles around an overall shape center.

The general algorithm used is similar for both types of programs. First, the algorithm requires basic information to geometrically describe the shapes in the X-Y plane. A shape with vertices is described by the location of those vertices: three for triangles and two opposing vertices for squares and rectangles. Circles are described by a given radius and central coordinates. After selecting a shape and entering a geometric description, the area bound by the shape is marked to be ablated or to be protected from ablation. For example, this allows for the creation of a recessed square pattern by direct ablation or a square island of material by ablating outside of the square instead. The program tests every point within the user-defined test region to find the appropriate coordinates corresponding to the set of given shapes and their preferences for ablation. After establishing each shape, a preview pattern is updated to display the latest appearance of the overall design and increasingly complex designs are developed by adding more shapes. Once the design is complete, the preview pattern is written to an Excel™ file as a list of coordinate points. An example design is displayed in Figure 13. This pattern was created by overlaying four rectangles and ablating points within any of the four shapes.

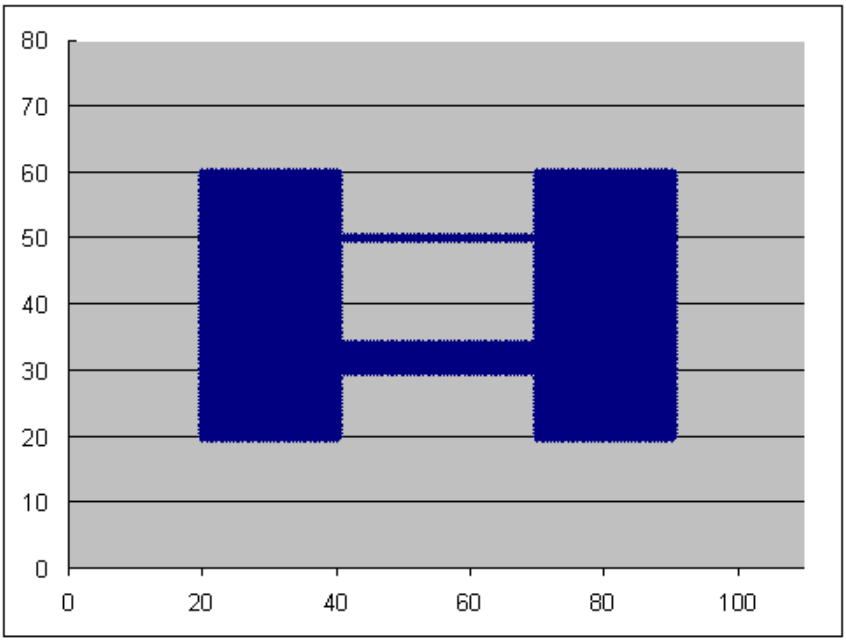

Figure 13. Superposition design. This microstructure was created by the addition of two large, wide rectangles and two thin, long rectangles. The blue space in this image is to be ablated and the scale is in μm.

The rotation program allows for the creation of complex designs by the use of a rotation algorithm. In this program, a simple shape is constructed with an orientation parallel to the positive X axis, and the overall shape center and angles of rotation are specified. The angles describe the amount of rotation the base shape will experience with reference to the overall shape center as the axis of rotation. To test the points, the X-Y plane is rotated by the negative of the given angles. With each rotation, the rotated space is compared to the reference shape and the appropriate points in actual space are added to the preview shape. Multiple additions of the rotated base shape create the overall design. For example, Figure 14 shows a star shape created by placing a rotated triangle at 0, 90, 180, and 270 degrees with respect to the shape center.

3.4. Procedures

There are several important procedures involved in the ablation of micropatterns. The first step is to clean new samples in an ultrasonic cleaner with acetone and then methanol for five minutes each. Relatively large samples are secured on the nanostage by the surface tension from a drop of methanol placed between the sample and the stage. Extremely small samples are taped to a Scanning Electron Microscope (SEM) sample mount to minimize handling and damage. Once the laser oscillator has mode-locked, the beam power is selected and the firing mode is set to a programmed repetition rate or to single shots. Next, the sample is placed under the laser objective by using the microstage program. To find the correct focus, the objective is manually scanned in Z towards the sample while viewing the current focal plane through the eyepiece. If the surface is not clearly visible, the objective is scanned towards the sample while ablating until a spot feature is created. The correct focus is achieved when the surface or surface debris is clearly visible. To complete the ablation process, the desired micropattern is designed in the

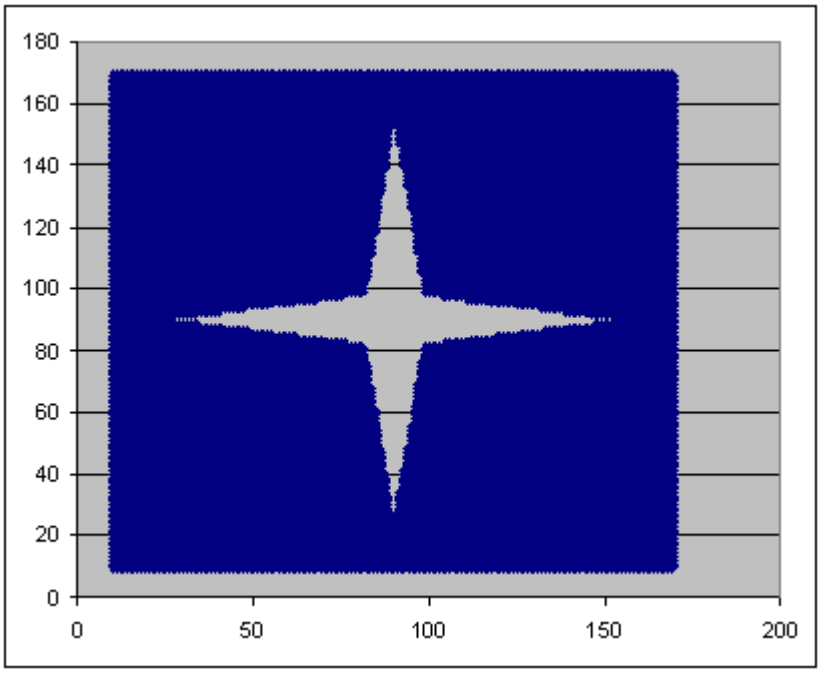

Figure 14. Rotation design. This star micropattern is created by ablating the area outside of four joined triangles rotated every 90 degrees.

nanostage program and ablation is initiated. Dr. Yelena White, Dr. Othman Zalloum, and the author performed the process of material ablation for the results shown in Chapter 4.

To perform Raman spectroscopy, some adjustments are required to the laser delivery system. The output of the Verdi V18 laser bypasses the Ti:S modules and is directed through an alternate beam path used specifically for Raman. Though both the ablation and the Raman beam paths are aligned for delivery, they can not be used simultaneously because both require the Verdi module's output. The Raman objective is then rotated into alignment to replace the ablation objective. A CCD photodetector collects the signal emitted from the sample and relays the spectrum to a computer for viewing and analysis. Dr. Othman Zalloum and the author performed Raman spectroscopy and the results were analyzed by Zalloum.

The depth of small holes created by femtosecond ablation cannot be measured by direct observation without heroic methods. Routine measurements of hole depths are made by replication with cellulose acetate. For the replication process, the ablated sample is cleaned for thirty minutes in acetone and methanol. Clean, ablated samples are mounted on SEM pegs using double-sided carbon tape. Acetone is placed on the sample, followed by a piece of cellulose acetate film from Electron Microscopy Sciences that has a thickness of 35 μm. The film is dissolved by the acetone and solidifies in the voids of the ablated pattern. After thirty minutes, the films are pulled off and mounted on a SEM peg as follows: SEM peg, double-sided carbon tape, glass microscope slide, double-sided carbon tape, replica film. The edges of the replica film are taped down with more carbon tape to make contact with the conductive SEM peg. Relatively small samples are mounted on a SEM peg using carbon tape with more tape placed near the edges of the sample. The original samples and the sample replicas are then coated with

platinum, gold, or carbon to ensure good conductivity. Examples of a gold-coated sample and replica are exhibited in Figures 15 and 16. An uncoated sample is shown in Figure 17.

Good conductivity is important for viewing with SEM, which is critical for the analysis process. By taking SEM micrographs of the samples and replicas, we can directly record the dimensions of the micropatterns created. These dimensions, such as hole diameter, hole or feature depth, or ablated edge roughness can by analyzed to find relationships between laser parameters for different materials or to give insight for the development of future micropatterns. Dr. Yelena White, Dr. Othman Zalloum, and the author composed the SEM images exhibited in this work.

3.5. Materials

The two materials machined in this work are two forms of diamond created by different techniques. Though both materials are diamond, it is important to recognize any differences in the process of creating micropatterns on the two materials. The single crystal diamonds were supplied by the Diamond Edge Company of Largo, Florida and were created by a high pressure, high temperature (HPHT) process. In this process, a diamond seed crystal assimilates surrounding graphite and grows under the applied pressure and temperature. This material is mostly transparent at the laser operating wavelength of 800 nm. The second diamond material, which is polycrystalline in nature, was provided by the Diamond Microelectronics Group [38, 39] at Vanderbilt University in Nashville, Tennessee and created by plasma enhanced chemical vapor deposition (PE-CVD). In this process, reactive gases are pumped into a chamber where an energy source creates a plasma to facilitate a chemical reaction and deposit carbon on a substrate. This material has a high content of sp^2 bonds and absorbs at the laser operating wavelength. The

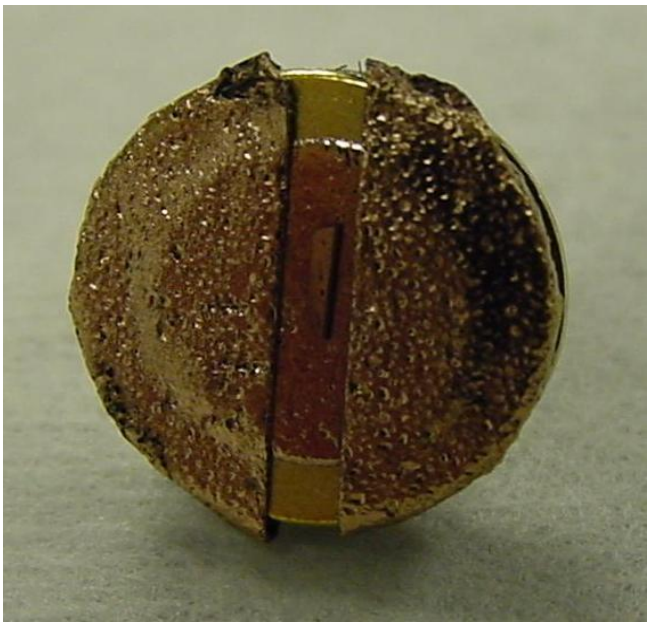

Figure 15. Single crystal diamond chip. The sample is the small chip in the center. The sample is secured to the sample mount by round carbon tape and strips of carbon tape are placed on either side. The samples are coated to improve conductivity.

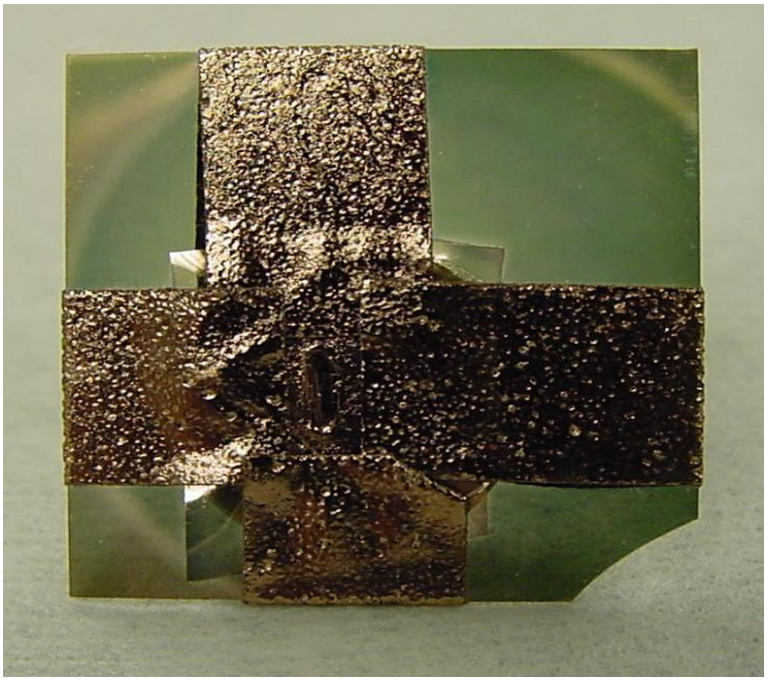

Figure 16. Sample replica. This gold-coated replica was created from the sample shown in Figure 15. The strips of carbon tape overlap all four sides to contact the base of the aluminum SEM peg to improve conductivity.

Figure 17. Polycrystalline diamond. This uncoated polycrystalline diamond sample is held at an angle. The black dots on the surface of the sample are machined features. The round carbon tape is visible under the sample.

differences in bonding and absorption will cause the two materials to have slightly different ablation processes and will generate noticeable variations in compared results.

4. Experimental Results

4.1. General Showcase of Designs

The following sections exhibit and discuss several of the micropatterns ablated on single crystal and polycrystalline diamond materials. Originally, the algorithms for constructing shapes did not exist and the variety of available designs for ablation was restricted to a few choices. The LabVIEW™ programs supported the creation of arrays, lines, and the letters "UTSI", as shown in Figures 18-20. Because the creation of arrays of holes was possible, so was the ability to form arrays of nanowires by using the replication technique. An example of an array of nanowires with an average height of approximately 10.4 μm is shown in Figure 21. In order to expand the number of shapes for ablation, we decided to take advantage of the same programming that allowed the UTSI shape to be imported into LabVIEW™ as a list of coordinate points. In a few of the results presented in this chapter, stray marks which were not projected by the designs were created on the sample by a malfunctioning shutter which would not completely close while the sample was moved between ablation sites.

We created a diverse range of new superimposed shapes constructed from several simple shapes. Figure 22 is the result of ablating outside of four identical and equally spaced squares on polycrystalline diamond. The two shapes displayed in Figures 23 and 24 for polycrystalline diamond show the two options for pattern ablation. Figure 23 shows the ablation within the limits given by three closely spaced triangles while Figure 24 shows the protection of the triangles but the ablation of all space outside of the triangles up to a maximum specified boundary. Figures 25 and 26 show a shape resembling a ladder ablated on both polycrystalline and single crystal diamond materials. This shape was created by superimposing two large rectangles with two long, thin rectangles resembling channels. Figures 27 and 28 show a star

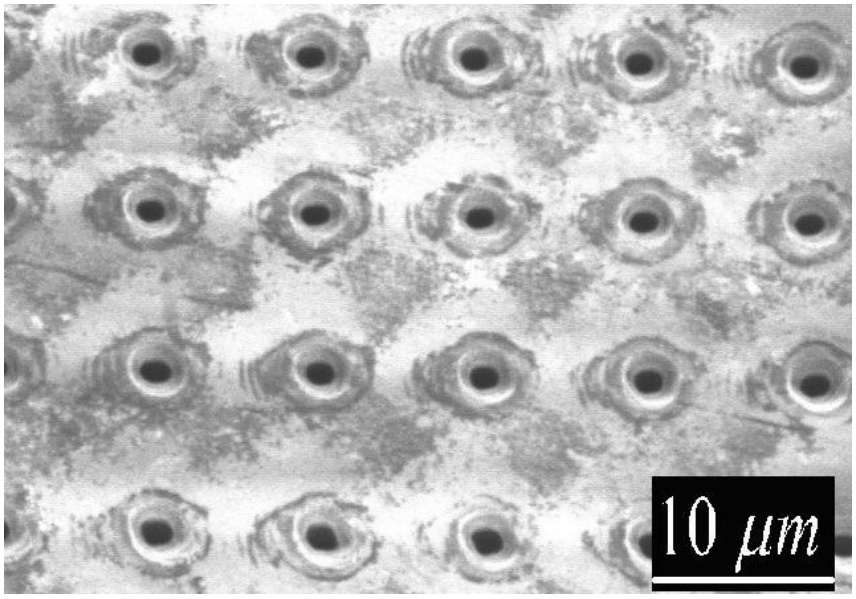

Figure 18. Array of holes. This array of holes on single crystal diamond was machined with 10 μm spacing between holes at a repetition rate of 250 kHz and a pulse energy of 0.4 μJ.

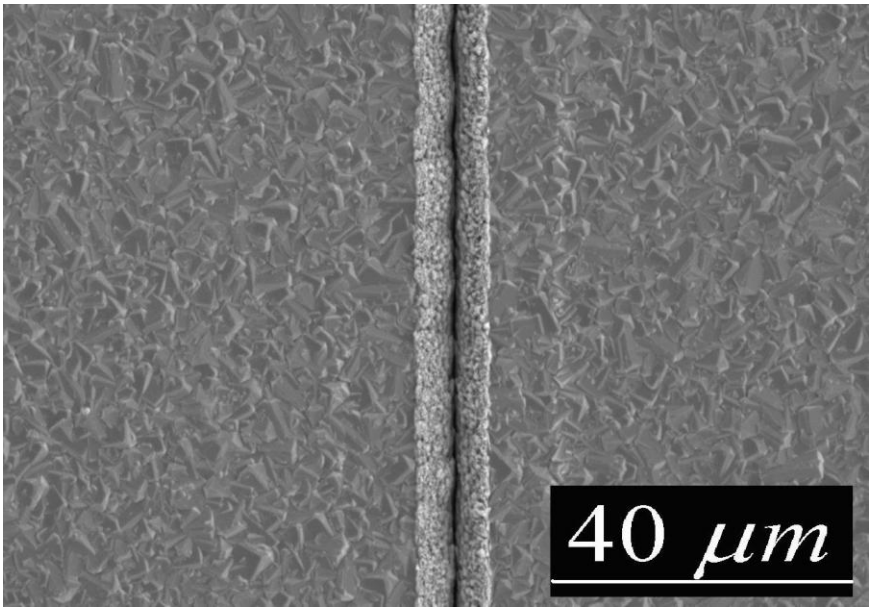

Figure 19. Line feature. This line was created on polycrystalline diamond by moving the microstage during ablation at 250 kHz.

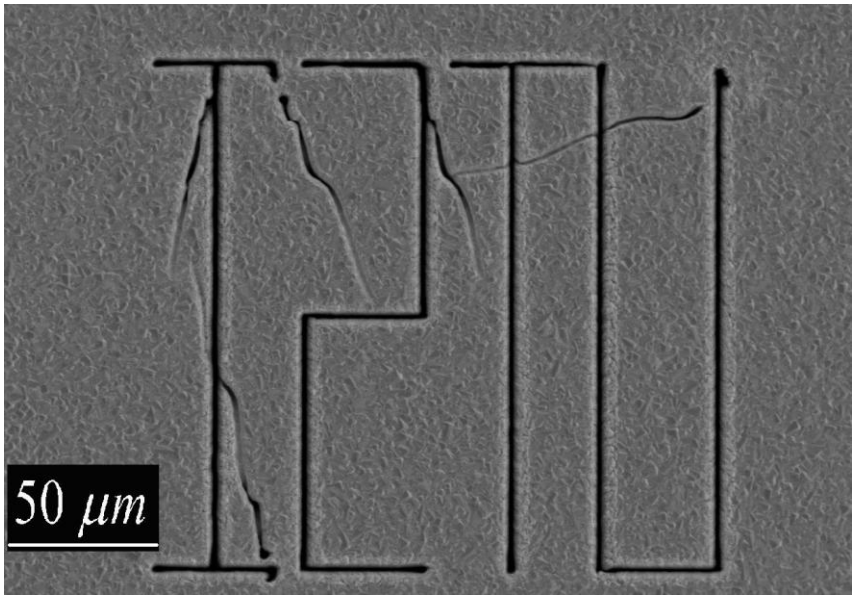

Figure 20. UTSI pattern. This UTSI pattern was ablated on polycrystalline diamond at 250 kHz with a pulse energy of 2.2 μJ. The design consists of many points placed in a row to form the lines of the letters. A replica of this pattern would spell "UTSI." Several unintended stray marks are visible.

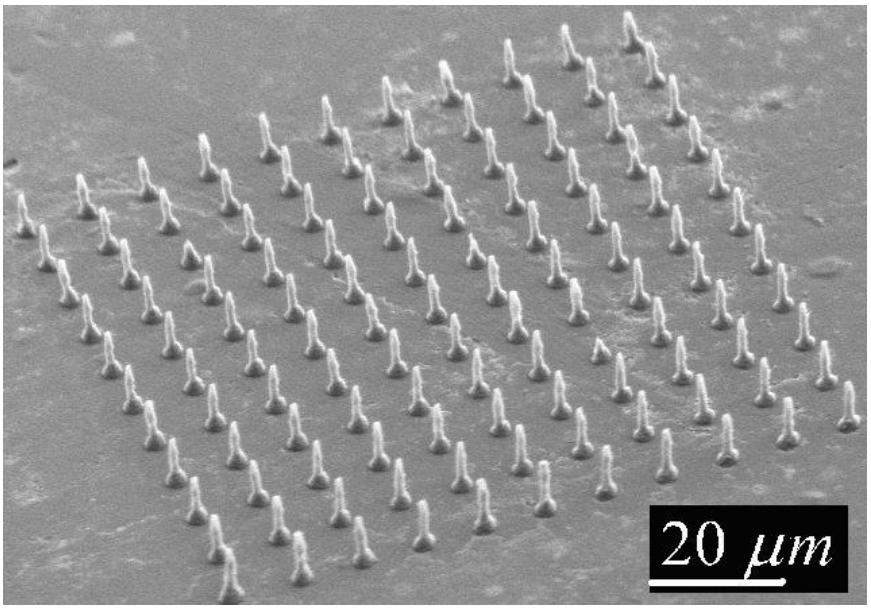

Figure 21. Array of nanowires. This pattern is the result of replicating the array shown in Figure 18. The height of the nanowiress measure approximately 10.4 μm.

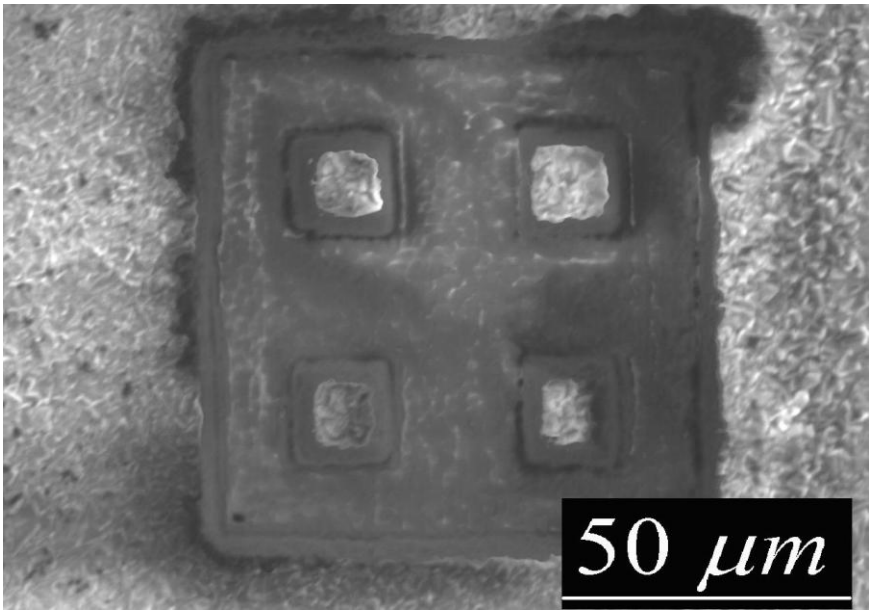

Figure 22. Ablation outside of squares. The ablation outside of four squares forms this pattern on polycrystalline diamond at 250 kHz and a pulse energy of approximately 1.4 μJ.

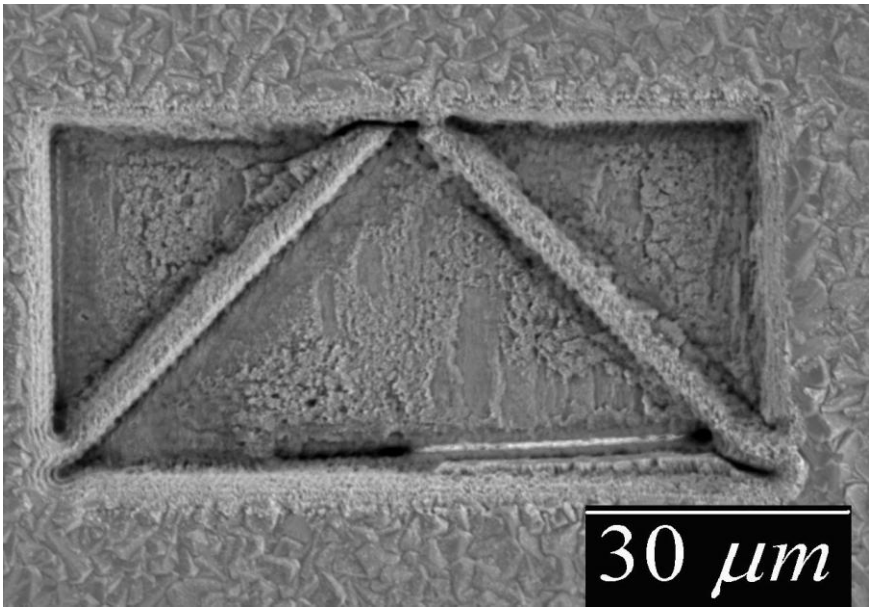

Figure 23. Ablation inside triangles. A pattern of three triangles ablated on polycrystalline diamond at 1.2 μJ and 250 kHz.

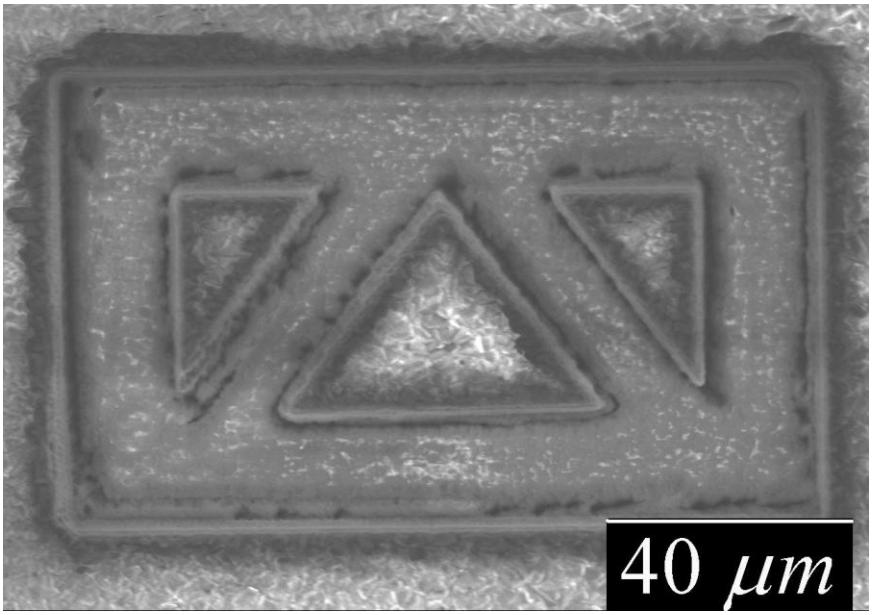

Figure 24. Ablation outside of triangles. The corresponding inverse pattern for Figure 23 ablated on polycrystalline diamond at 250 kHz and approximately 1.4 μJ.

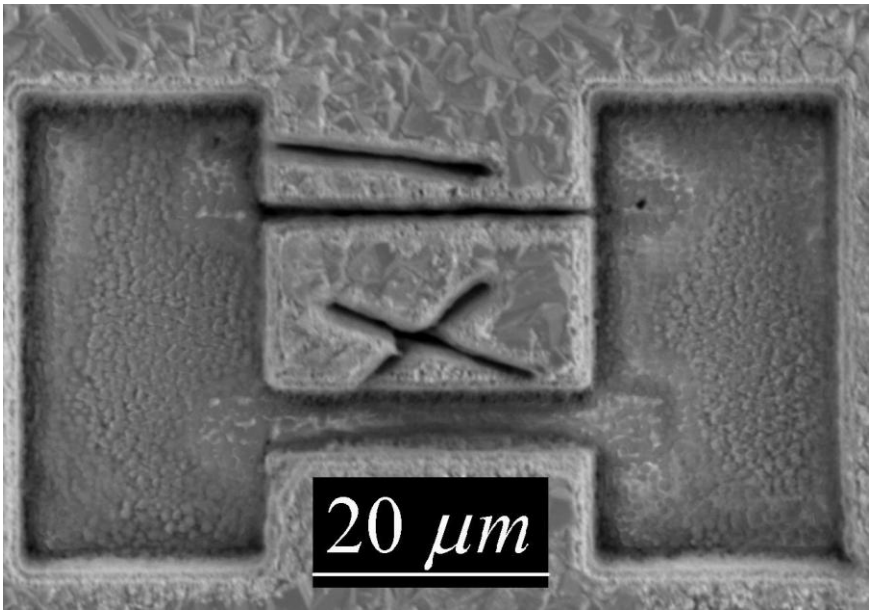

Figure 25. Polycrystalline diamond squares pattern. This pattern was created at 250 kHz and a pulse energy of 1.2 μJ. This image shows unintended stray marks created by a malfunctioning shutter.

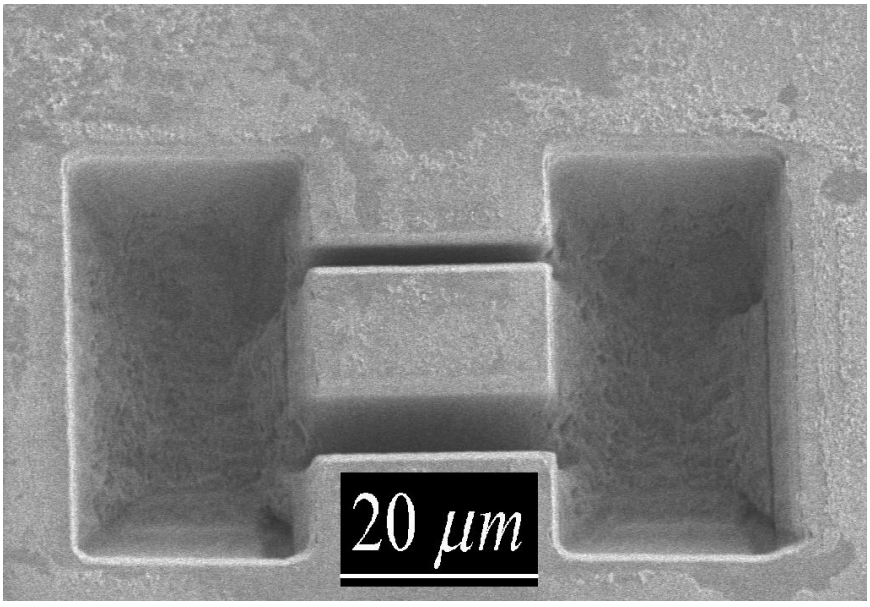

Figure 26. Single crystal diamond squares pattern. The same pattern shown in Figure 25 ablated on single crystal diamond at 250 kHz and 1.2 μJ.

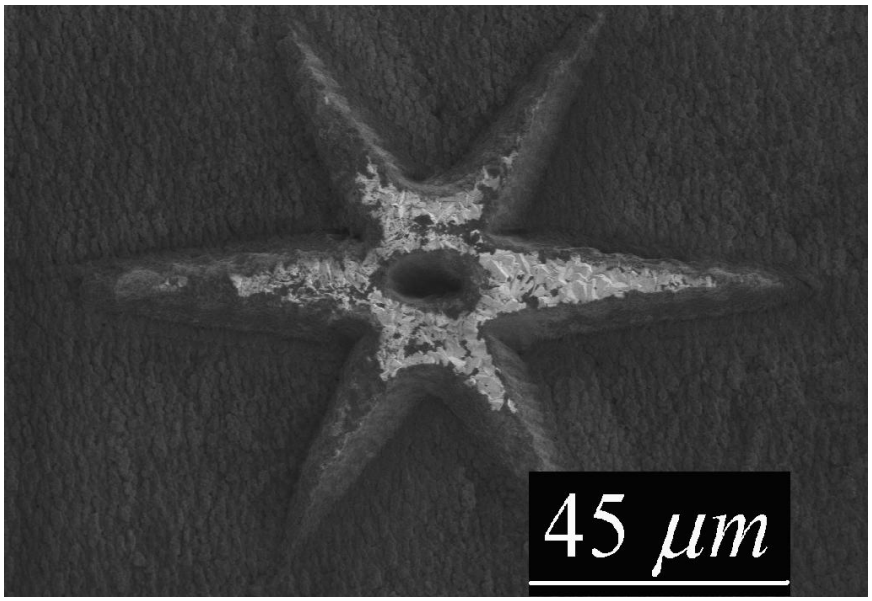

Figure 27. Straight polycrystalline star. This star pattern has six straight arms and an ablated center hole created on polycrystalline diamond at 250 kHz and 1.6 μJ.

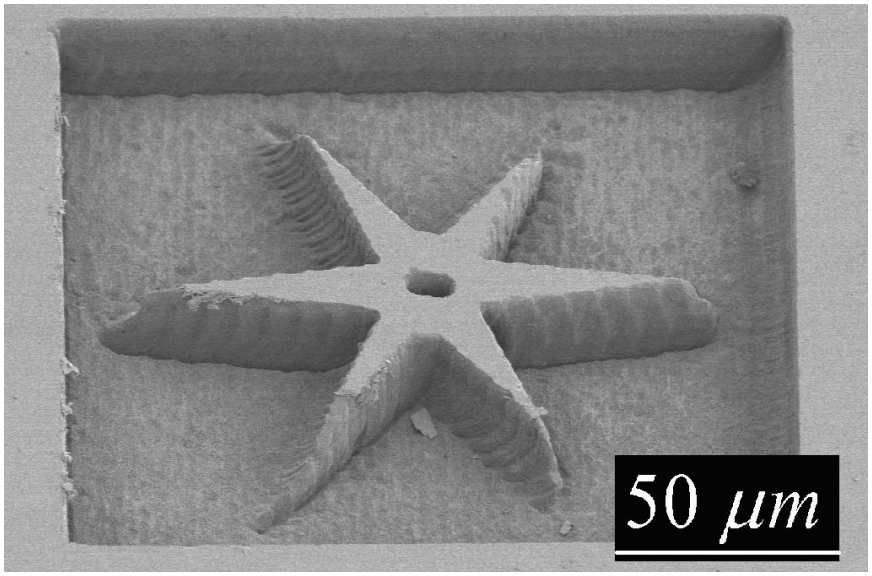

Figure 28. Straight single crystal diamond star. The same design presented in Figure 27 except ablated on single crystal diamond at 250 kHz and 1.4 μJ.

shape with six identical straight arms created by the rotation algorithm for both material types. The combination of an ablated center hole and several protected triangles rotated and equally spaced create this star shape. Figures 29 and 30 show another star shape ablated on the two diamond materials. The reference shape for this design was bounded by a circle, an ellipse, and a line to form a single arm of the overall shape and then rotated every 90 degrees. A small hole was added to the center of the design to be ablated. When ablated in single crystal diamond, the feature presented in these figures is approximately 8.1 μm, or 65 percent, deeper than the polycrystalline depth of 12.6 μm.

After reviewing the experimental results, it is apparent that the ablation of the polycrystalline diamond material typically results in the formation of features with sloped walls. In contrast, the ablation of the single crystal diamond under similar experimental parameters creates deeper features with steep, vertical walls.

4.2. Examples of Design Improvements

Over the course of developing different shapes, we made improvements to a few of the original designs. One of our first designs is shown below in Figure 31. We created a star shape by superimposing four triangles around a common center to be protected and adding a small center hole to be ablated. Figure 32 shows that the actual result of ablation on a single crystal diamond sample did not follow the design as intended and was therefore an unsatisfactory result. The problem with the original design is that the ablated area was larger than intended. The ablated area "leaked" over its boundaries and the smallest features at the edges of the design were completely lost. To create the desired star shape, a better design was developed and is shown in Figure 33 while the resulting feature is shown in Figure 34. The changes included

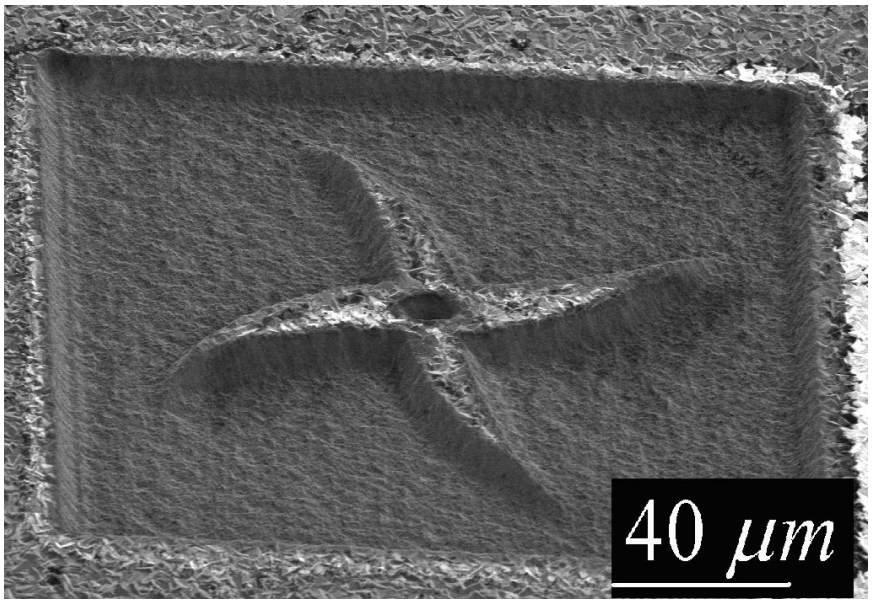

Figure 29. Curved polycrystalline diamond star. This star pattern has four curved arms ablated on polycrystalline diamond at 250 kHz and 1.2 μJ. The depth of this feature is approximately 12.6 μm.

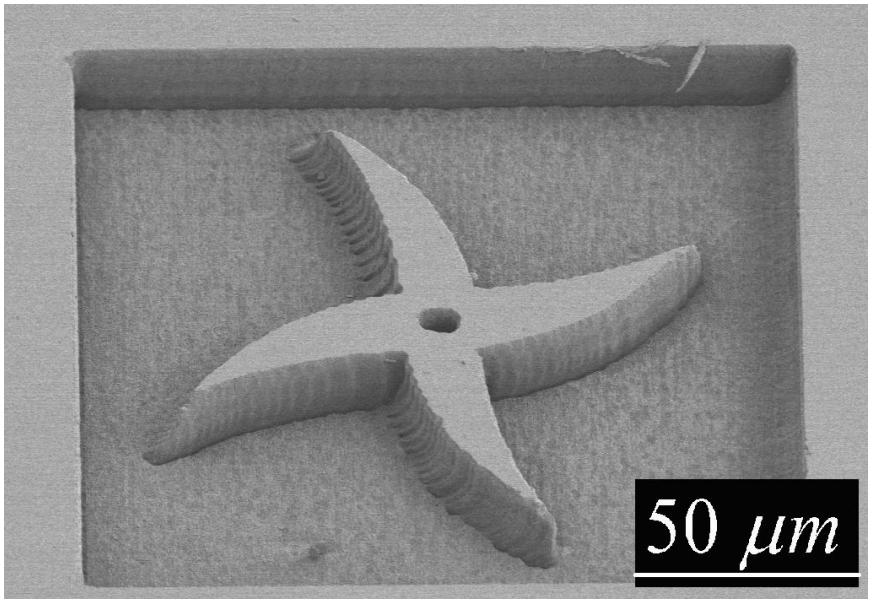

Figure 30. Curved single crystal diamond star. The same design as shown in Figure 29 ablated on single crystal diamond at 1.4 μJ. The depth of this feature is approximately 20.7 μm.

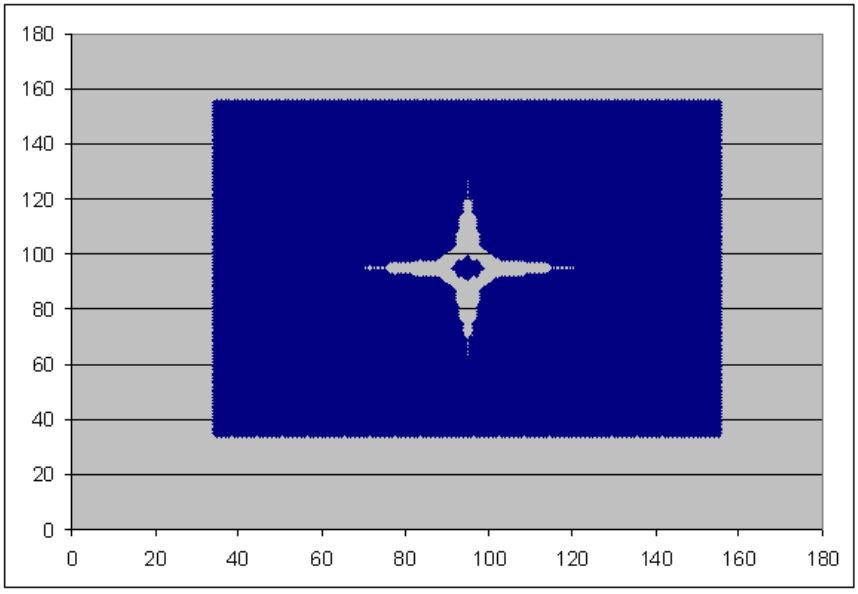

Figure 31. Original star design. The original star design produced by our superposition program.

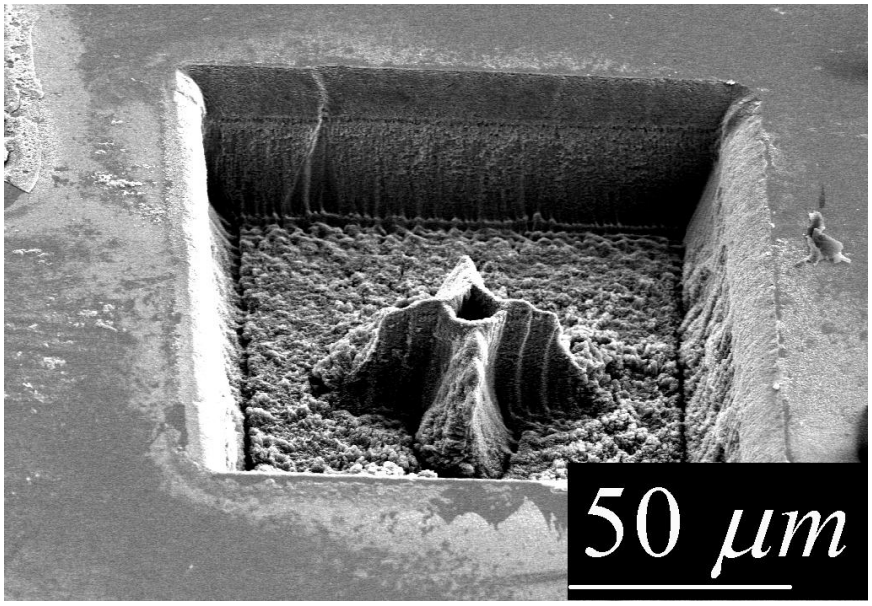

Figure 32. Original design results. The design shown in Figure 31 failed to adequately reproduce the design on single crystal diamond. The feature is shown at a 45 degree tilt.

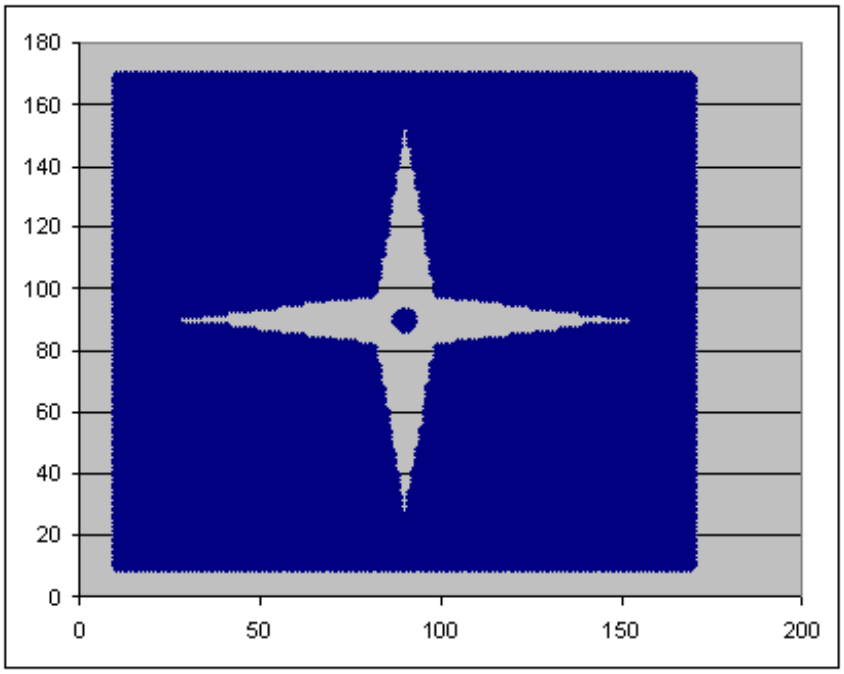

Figure 33. New star design. A much larger and improved version of the design shown in Figure 31.

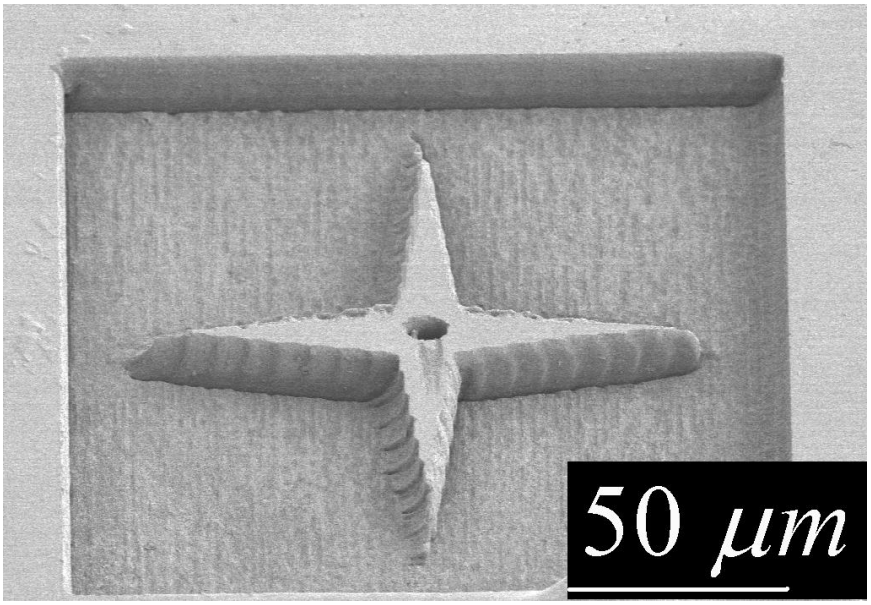

Figure 34. New design results. This result of the improved star design was ablated on single crystal diamond at 250 kHz and 1.4 μJ.

creating longer triangles with a wider base to anticipate the "overflow" of the ablated area. Comparing the two designs with their respective results shows that the shape in Figure 34 looks much more like its intended design than the result shown in Figure 32.

A more recent design improvement is shown below for the collection of triangles ablated on single crystal diamond in Figure 35. The shape was created by superimposing four triangles so that the lower vertices overlapped slightly. The original results shown in Figure 36 exhibit jagged boundary lines due to the resolution the algorithm used to test and build the shape. The original programming resolution correlating to Figure 36 was set to one increment in test space equal to one micrometer in actual space. Figures 35 and 37 are results of the improved resolution of one increment per 0.5 micrometers. Examination of Figures 36 and 37 shows the noticeable difference between the jagged steps of the old resolution and the much smoother lines created by the new resolution. The majority of our created shapes were designed with the original resolution. In most cases, the original resolution is satisfactory and the redevelopment of the shape is unnecessary.

4.3. Variation of Feature Dimensions with Power

Since the average power of the laser output is an important variable in the ablation process, it is natural to wonder if there is a variation of ablated features with respect to different levels of power. Arrays of holes ablated on both polycrystalline and single crystal diamond samples were created at various powers at a repetition rate of 250 kHz. Figure 38 shows an example of an array of holes ablated on a polycrystalline sample with a pair of white lines marking the measurement of the surface diameter of the hole. This measurement was repeated

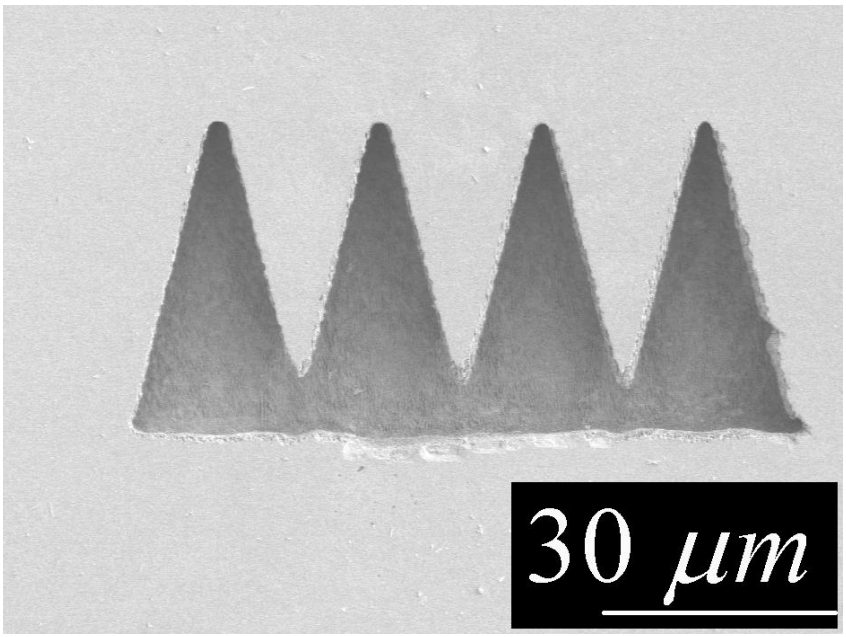

Figure 35. Multiple triangle design. A design created by four overlapping triangles ablated onto single crystal diamond at 2.4 μJ.

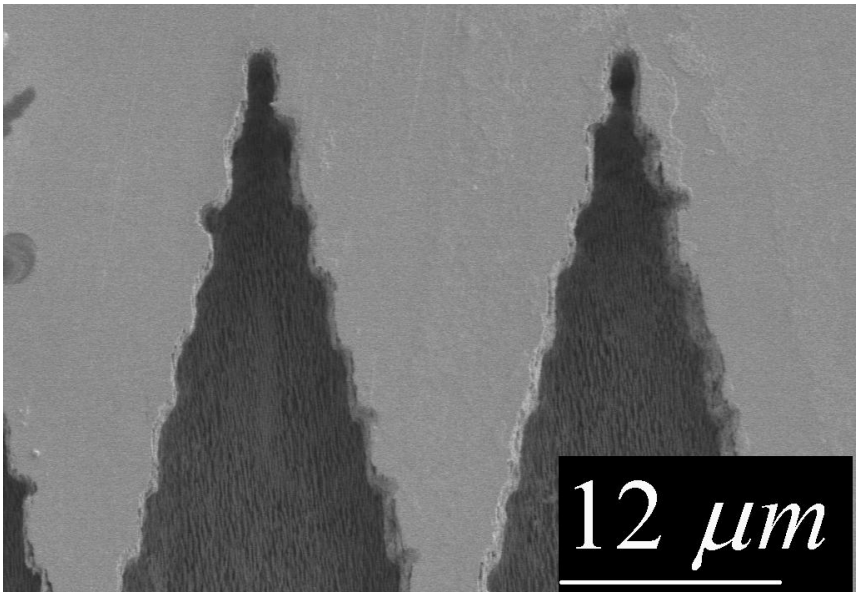

Figure 36. Old resolution result. This result was ablated on single crystal diamond using the old resolution with a laser pulse energy of 1.4 μJ.

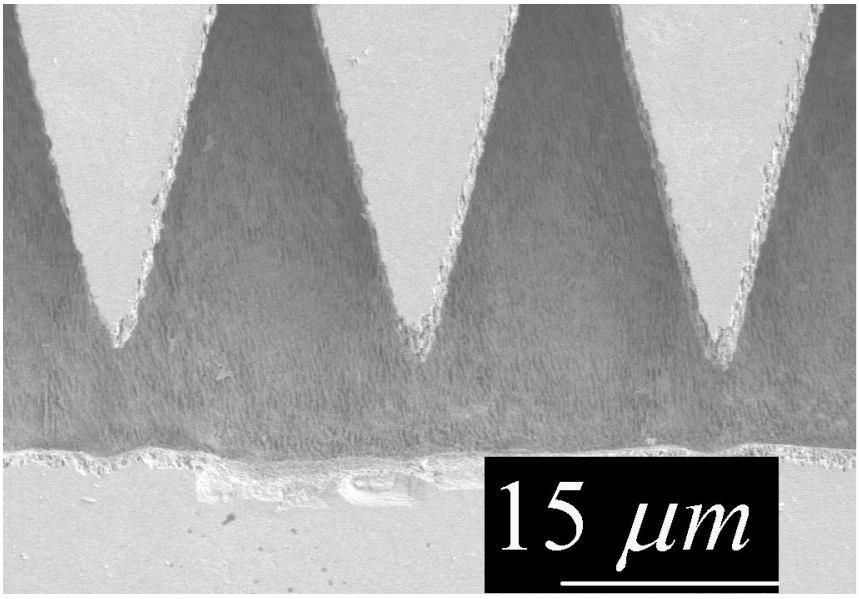

Figure 37. New resolution result. A magnified image of the same design shown in Figure 35. The lines are much smoother for this resolution when compared to the result of the last figure.

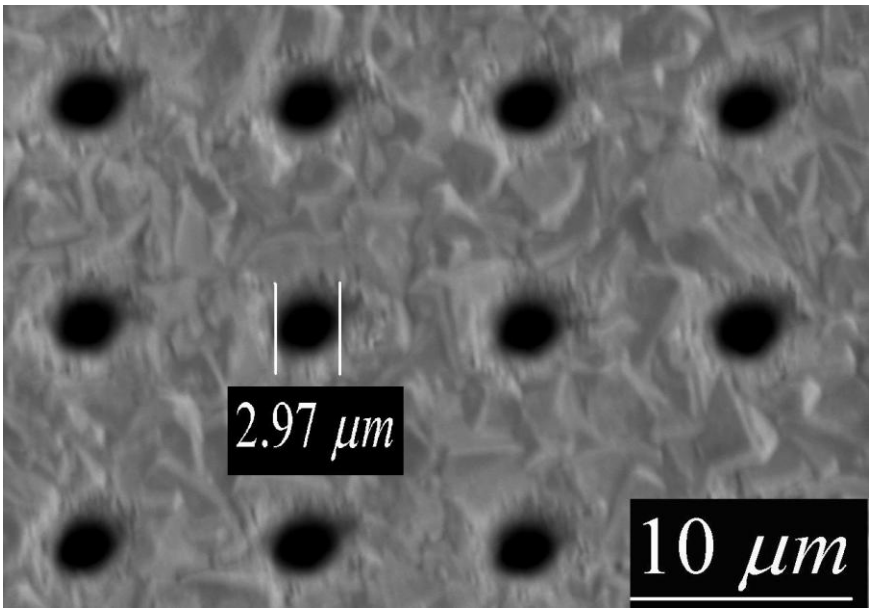

Figure 38. Entrance hole diameter measurement. This array of holes was ablated in polycrystalline diamond at 250 kHz and 2.2 μJ. The white lines mark the measurement taken to form the data presented in Figure 39.

for several holes in a single array and averaged. The resulting entrance hole diameters are plotted versus laser pulse energy in Figure 39. Overall, the entrance hole diameters for both materials are approximately linear with increasing power. At every power measured, the holes from the single crystal diamond were larger than those of the polycrystalline diamond.

The shape constructed of multiple triangles exhibited above in Figure 35 was the second pattern analyzed for feature variation with changing power. Figure 40 is a magnified image of the gap between two unablated sections of the shape. This figure shows two sets of black lines representing the two measurements of the gap length taken for the analysis. The measurement on the left is the distance between the two unablated surfaces forming the gap. The second measurement is the minimum distance between the partially ablated bulk on either side of the gap. Figure 41 shows the results of these two measurements versus a range of laser powers ablated on single crystal diamond at a repetition rate of 250 kHz. The surface-surface measurement is longer than the edge-edge measurement for every measured power. This graph shows that the actual results of ablation deviate more from the shape design with increasing power and at a linear rate. Therefore, low power offers the best chance for the precise machining of micopatterns on the surface of single crystal diamond.

Figures 42 and 43 show the difference in ablation results for low and high power, respectively. A comparison between the two figures shows that the surface recedes more when ablating with a greater power. Overall, the two graphs suggest that the laser has a greater impact on the fringe areas around targeted sites as the laser output power increases. It is likely that the increase in the ablation of fringe areas is partially responsible for the unsatisfactory result of our original star shape created with the old resolution. It is possible that if we had ablated the original star design at a lower power, then the results may have been more successful.

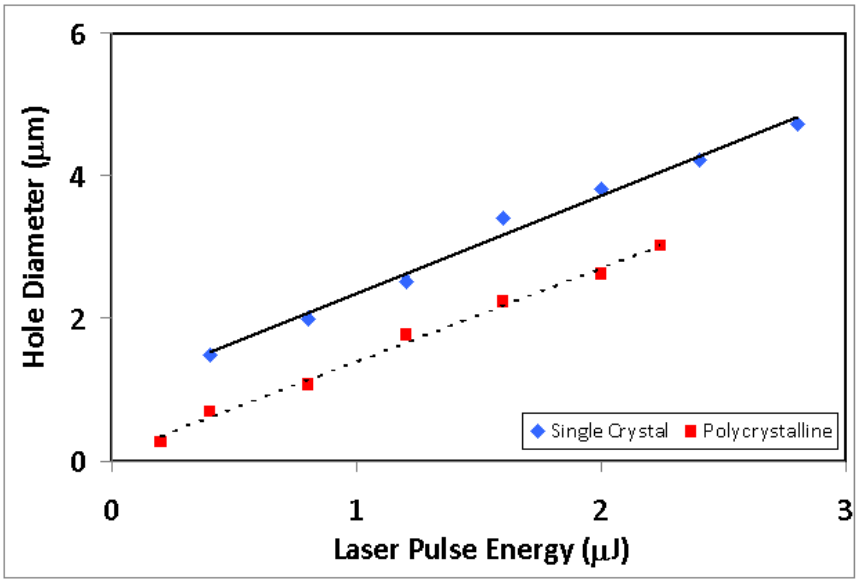

Figure 39. Entrance hole diameter versus power. Measurements of the surface diameter of holes are presented versus the power at which they were ablated. Though both materials have a linear dependence on increasing power, the single crystal diamond values are larger for all powers.

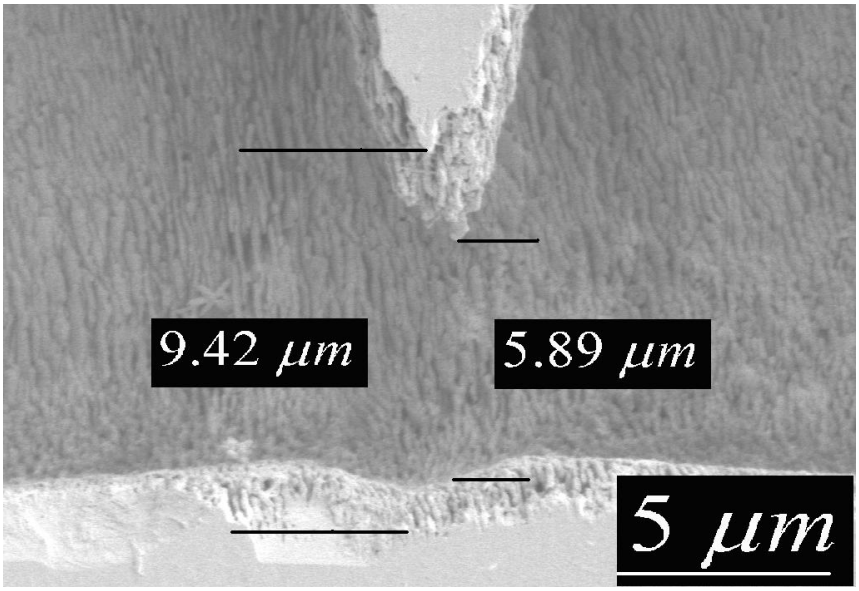

Figure 40. Gap distance measurement. This is a magnified image of the triangle structure shown in Figure 35. The two sets of lines represent the measurements of the gap distance taken for the analysis presented in Figure 41.

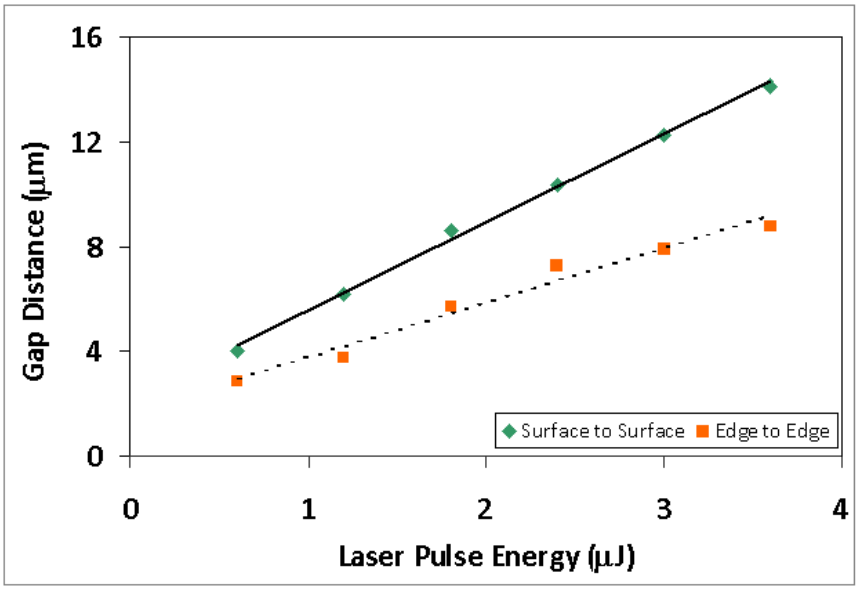

Figure 41. Gap distance versus power. This graph shows the measurements of the gap distance versus the power at which the features were ablated. Both measurements increase linearly with power with the surface-surface gap distance experiencing the faster rate of increase.

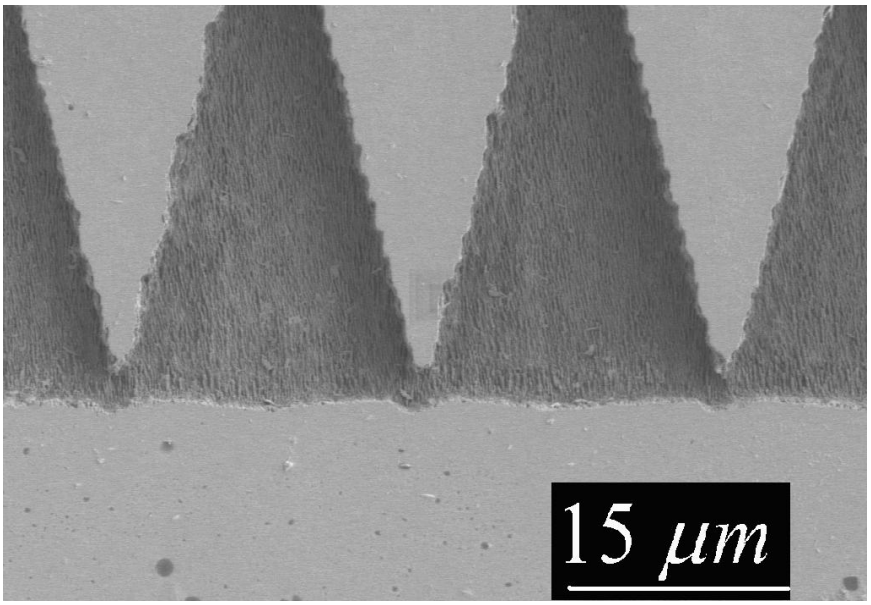

Figure 42. Gaps ablated at low power. This magnified image shows the three gaps of the multiple triangles pattern ablated on single crystal diamond at 250 kHz and a low laser pulse energy of 0.6 μJ.

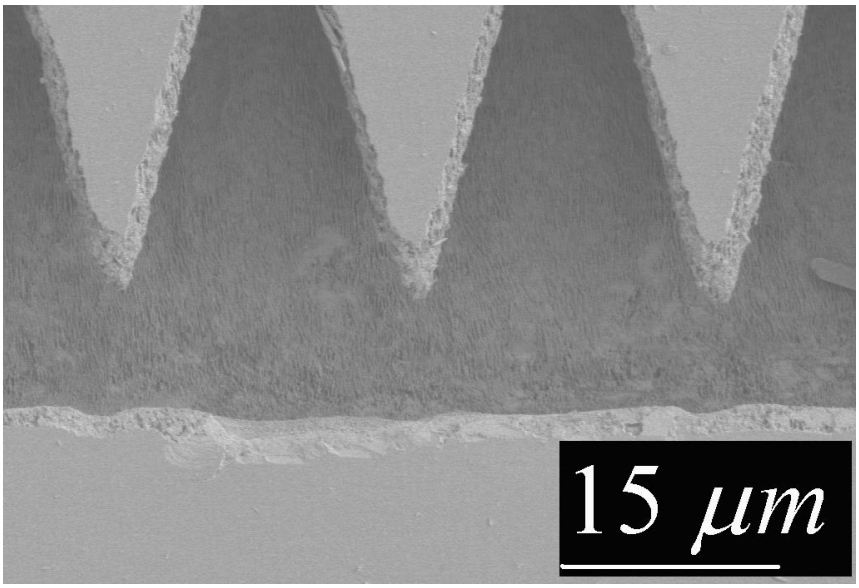

Figure 43. Gaps ablated at high power. These features were created at the same conditions as those in Figure 42 except ablated at a much higher laser pulse energy of 3.6 μJ. Note the difference in the gap distance between the two images.

4.4. Raman Spectroscopy of Ablated Regions

Raman spectroscopy of our single crystal diamond sample is the last topic of interest concerning the machining of diamond materials. By performing Raman spectroscopy in ablated regions, we are looking for the peaks in the Raman spectra which are associated with graphite, as shown in Figure 44. The presence of these peaks in the spectra suggests that some of the diamond has converted to the graphite form and that the resulting material is not purely diamond.

Raman spectroscopy was performed on a single crystal diamond sample on a pattern similar to the one shown in Figure 45. This pattern has two large ablated regions located at the top and bottom of the image with a section of vertical lines in between them. An un-ablated region is shown to the left of the pattern for contrast. Figures 46 and 47 show magnified images of the un-ablated and ablated areas, respectively. Figure 48 shows the typical Raman spectrum obtained from our single crystal diamond experiments. The black line with higher intensity is the signal acquired from an un-ablated or un-irradiated area and the less intense, red line is the result from scanning an ablated or irradiated region. Figure 48 shows that the peaks which indicate that graphite has formed is not present and that the peak associated with the bonding of diamond did not shift or broaden. Therefore, the ablated diamond region is still diamond and did not graphitize. The only noticeable difference between the two peaks is that the intensity from the ablated region is around half of the intensity acquired from the unablated region. This drop in intensity is attributed to scattering of the Raman signal at the surface of the ablated region by nanoscale features like those shown in Figure 47. Using Raman spectroscopy, we have shown that the creation of micropatterns through laser ablation with our laboratory setup does not cause graphitization of single crystal diamond samples.

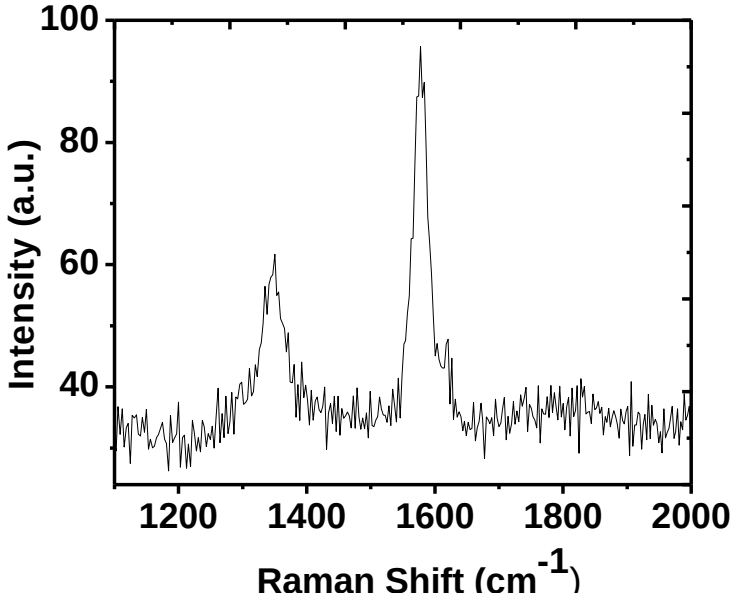

Figure 44. Raman spectrum of graphite. This spectrum for graphite was obtained by the integrated Raman setup. The two peaks shown are the D peak at ~1350 cm^{-1} and the G peak at ~1580 cm^{-1}.

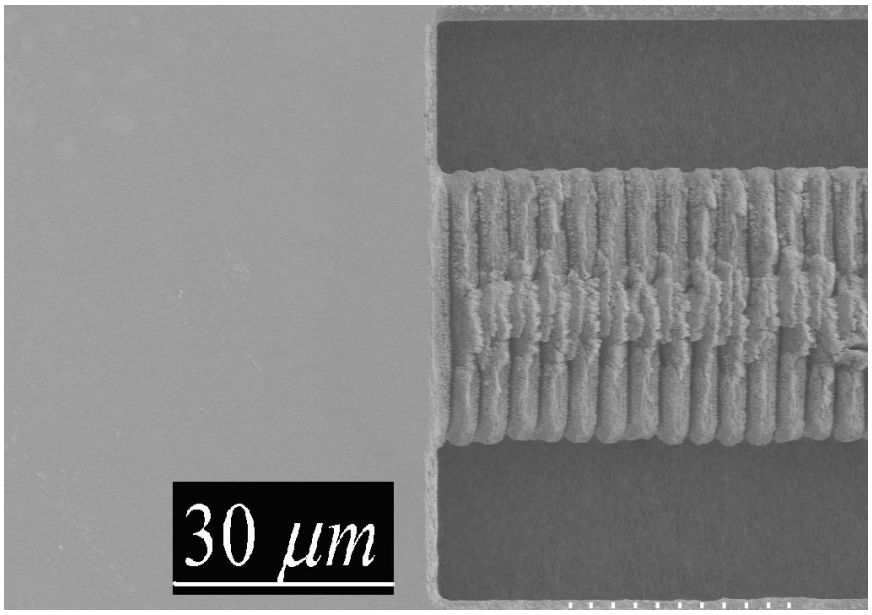

Figure 45. Block and lines pattern. This pattern is composed of rectangles and lines ablated on single crystal diamond at 1.2 μJ and 250 kHz. This image shows part of the pattern on the right along with a large un-ablated region to the left.

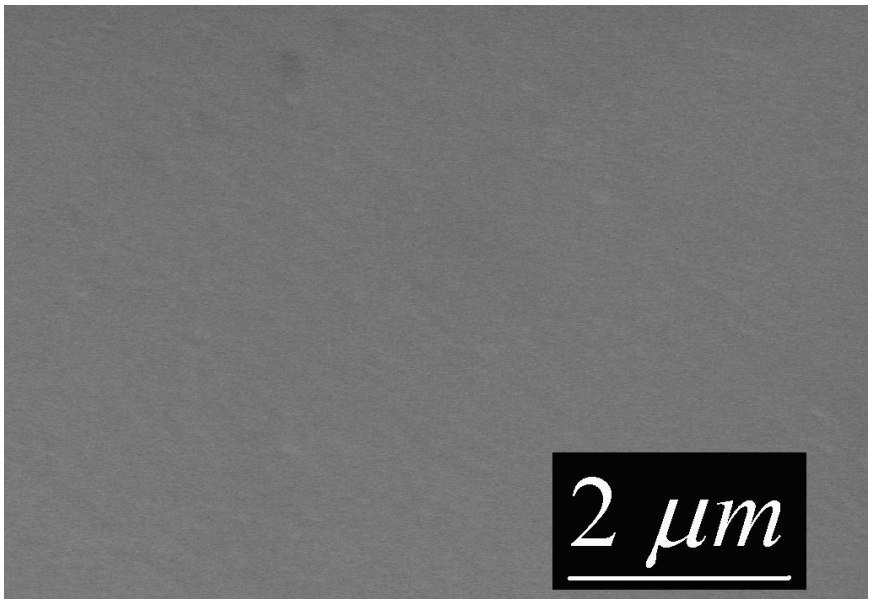

Figure 46. Un-ablated surface. A magnified image of the un-ablated surface of single crystal diamond is shown.

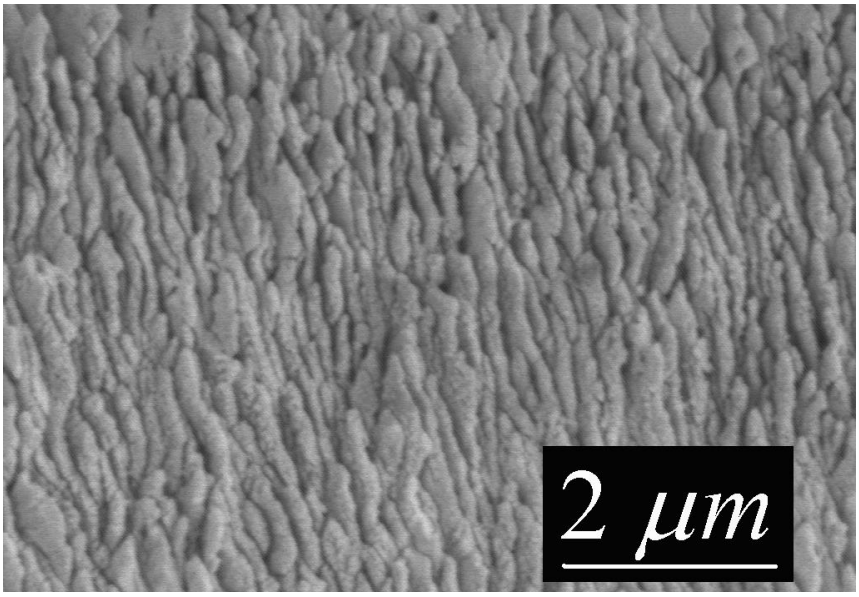

Figure 47. Ablated surface. This figure shows a magnified image of the surface texture within the ablated region of single crystal diamond. Nanoscale features like those shown here are responsible for the scattering of the Raman signal and the loss of intensity seen in Figure 48.

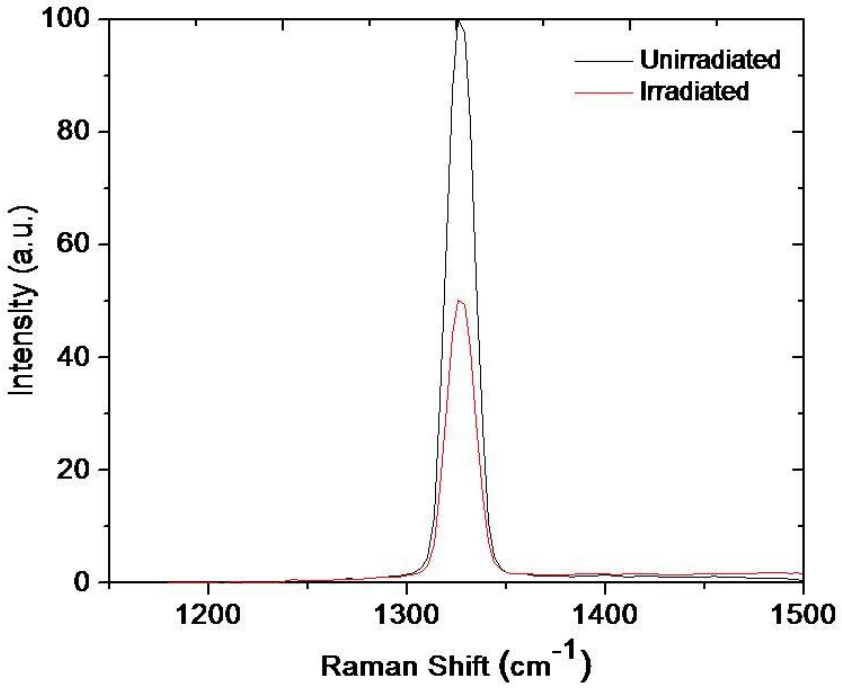

Figure 48. Raman results for single crystal diamond. The typical result for our Raman experiments involving ablated regions of single crystal diamond. The large, black graph shows the intensity of the Raman signal gathered from an un-ablated or un-irradiated area. The small, red graph shows the intensity acquired from an ablated region of the material. The peaks are located at ~1330 cm^{-1}.

5. Conclusions

It has been demonstrated that our programs can design patterns to create micrometer-sized features on diamond materials through femtosecond laser ablation. The results of our designs include a general showcase of patterns created on PE-CVD polycrystalline diamond and HPHT single crystal diamond by the superimposition and rotation of several simple shapes. Design improvements suggest that a higher resolution pattern will have smoother features and that the overextension of the ablated region should be taken into account during the pattern designing process. An analysis of the variance of feature dimensions with increasing power reveals that ablation of polycrystalline diamond produces features that are smaller and more shallow when compared to the features created on single crystal diamond. Also, increasing the power causes the sample's un-ablated surface at the feature boundary to recede. All of the measured dimensions exhibited in this work linearly increase with greater power for both materials. Overall, the most precise emulation of design is obtained when ablating with relatively low energy. Also, we have used Raman spectroscopy to show that the ablation of single crystal diamond does not cause a material conversion to graphite and that the only difference between the ablated and un-ablated scans is a drop in intensity due to the scattering of the Raman signal by nanoscale surface features within the ablated region. Thus, we have shown that the creation of micropatterns on diamond materials by femtosecond laser ablation can have a high resemblance to the original patterns designed.

References

1. Zoubir, A., et al., *Practical uses of femtosecond laser micro-materials processing.* Applied Physics a-Materials Science & Processing, 2003. **77**(2): p. 311-315.
2. Liu, X., D. Du, and G. Mourou, *Laser ablation and micromachining with ultrashort laser pulses.* Ieee Journal of Quantum Electronics, 1997. **33**(10): p. 1706-1716.
3. Farson, D.F., et al., *Femtosecond laser micromachining of dielectric materials for biomedical applications.* Journal of Micromechanics and Microengineering, 2008. **18**(3).
4. Cheng, J.Y., et al., *Crack-free direct-writing on glass using a low-power UV laser in the manufacture of a microfluidic chip.* Journal of Micromechanics and Microengineering, 2005. **15**(6): p. 1147-1156.
5. Kim, T.N., et al., *Femtosecond laser-drilled capillary integrated into a microfluidic device.* Applied Physics Letters, 2005. **86**(20).
6. Joglekar, A.P., et al., *Optics at critical intensity: Applications to nanomorphing.* Proceedings of the National Academy of Sciences of the United States of America, 2004. **101**(16): p. 5856-5861.
7. Joglekar, A.P., et al., *A study of the deterministic character of optical damage by femtosecond laser pulses and applications to nanomachining.* Applied Physics B-Lasers and Optics, 2003. **77**(1): p. 25-30.
8. Gamaly, E.G., et al., *Ablation of solids by femtosecond lasers: Ablation mechanism and ablation thresholds for metals and dielectrics.* Physics of Plasmas, 2002. **9**(3): p. 949-957.
9. Bloember.N, *Laser-Induced Electric Breakdown in Solids.* Ieee Journal of Quantum Electronics, 1974. **QE10**(3): p. 375-386.

10. Korte, F., et al., *Three-dimensional nanostructuring with femtosecond laser pulses.* Ieee Transactions on Nanotechnology, 2004. **3**(4): p. 468-472.

11. Campbell, S., et al., *Single-pulse femtosecond laser machining of glass.* Journal of Optics a-Pure and Applied Optics, 2005. **7**(4): p. 162-168.

12. Gattass, R.R., L.R. Cerami, and E. Mazur, *Micromachining of bulk glass with bursts of femtosecond laser pulses at variable repetition rates.* Optics Express, 2006. **14**(12): p. 5279-5284.

13. Glezer, E.N. and E. Mazur, *Ultrafast-laser driven micro-explosions in transparent materials.* Applied Physics Letters, 1997. **71**(7): p. 882-884.

14. Tan, B., et al., *Laser drilling of thick material using femtosecond pulse with a focus of dual-frequency beam.* Optics and Laser Technology, 2003. **35**(3): p. 199-202.

15. *Properties*. [cited 2009 7/9/09]; Available from: http://www.diamond-materials.de/properties_en.htm.

16. Spear, K.E. and J.P. Dismukes, eds. *Synthetic Diamond: Emerging CVD Science and Technology*. The Electrochemical Society Series. 1994, Wiley-Interscience. 663.

17. Kononenko, T.V., et al., *Microstructuring of diamond bulk by IR femtosecond laser pulses.* Applied Physics a-Materials Science & Processing, 2008. **90**(4): p. 645-651.

18. Gomez, D., et al., *Femtosecond laser ablation for microfluidics.* Optical Engineering, 2005. **44**(5).

19. Li, X., et al. *Fabrication and Characterization of Nanofluidics Device Using Fused Silica for Single Protein Molecule Detection*. in *Materials and Processes for Medical Devices*. 2007.

20. Diez-Blanco, V., et al., *Deep subsurface waveguides with circular cross section produced by femtosecond laser writing.* Applied Physics Letters, 2007. **91**(5).

21. Ferrer, A., et al. *Deep subsurface optical waveguides produced by direct writing with femtosecond laser pulses in fused silica and phosphate glass*. 2007.

22. Mauclair, C., et al., *Ultrafast laser writing of homogeneous longitudinal waveguides in glasses using dynamic wavefront correction.* Optics Express, 2008. **16**(8): p. 5481-5492.

23. Liou, Y.L., et al. *Fabrication and field emission properties of ultra-nanocrystalline diamond lateral emitters*. 2008.

24. Subramanian, K., et al. *Nanodiamond lateral field emitter devices on thick insulator substrates for reliable high power applications*. 2008.

25. Tzeng, Y.F., et al., *Fabrication of an ultra-nanocrystalline diamond-coated silicon wire array with enhanced field-emission performance.* Nanotechnology, 2007. **18**(43).

26. *Products*. [cited 2009 7/9/09]; Available from: http://www.ussynthetic.com/index.php/site/products.

27. *High Quality Diamond Knives*. [cited 2009 7/9/09]; Available from: http://www.diamondedgeco.com/11533.

28. Ameer-Beg, S., et al. *Femtosecond laser microstructuring of materials*. 1998.

29. Schaffer, C.B., et al., *Micromachining bulk glass by use of femtosecond laser pulses with nanojoule energy.* Optics Letters, 2001. **26**(2): p. 93-95.

30. Gattass, R.R. and E. Mazur, *Femtosecond laser micromachining in transparent materials.* Nature Photonics, 2008. **2**(4): p. 219-225.

31. Perelomov, A.M., V.S. Popov, and M.V. Terentev, *Ionization of Atoms in an Alternating Electric Field.* Soviet Physics Jetp-Ussr, 1966. **23**(5): p. 924-&.

32. Yudin, G.L., et al., *Hole-assisted energy deposition in clusters and dielectrics in multiphoton regime.* Laser Physics, 2004. **14**(1): p. 51-56.

33. Bhardwaj, V.R., et al. *Strong field ionization inside transparent solids*. 2006.

34. Das, D.K., et al., *Femtosecond pulsed laser damage characteristics of 7% Y2O3-ZrO2 thermal barrier coating.* Applied Physics a-Materials Science & Processing, 2008. **91**(3): p. 421-428.

35. Horn, I. and F. von Blanckenburg, *Investigation on elemental and isotopic fractionation during 196 nm femtosecond laser ablation multiple collector inductively coupled plasma mass spectrometry.* Spectrochimica Acta Part B-Atomic Spectroscopy, 2007. **62**(4): p. 410-422.

36. Jee, Y., M.F. Becker, and R.M. Walser, *Laser-Induced Damage on Single-Crystal Metal-Surfaces.* Journal of the Optical Society of America B-Optical Physics, 1988. **5**(3): p. 648-659.

37. Ashkenasi, D., et al., *Surface damage threshold and structuring of dielectrics using femtosecond laser pulses: the role of incubation.* Applied Surface Science, 1999. **150**(1-4): p. 101-106.

38. Kang, W.P., et al. *Diamond vacuum field emission devices.* 2004.

39. Subramanian, K., et al. *Enhanced electron field emission from micropatterned pyramidal diamond tips incorporating CH4/H-2/N-2 plasma-deposited nanodiamond*. 2006.

Vita

Matthew David Parrish was born in Joelton, Tennessee. He received his undergraduate degree in Physics with minors in Applied Mathematics and Philosophy at Lipscomb University in Nashville, Tennessee in May 2007. Since then, he has been working towards a Master of Science degree in Material Science and Engineering at the University of Tennessee Space Institute (UTSI) in Tullahoma, Tennessee.